



## Experimental analysis and thermodynamic modeling for multilevel heat exchange system with multifluid in aero engines

Weitong Liu <sup>a,b,c</sup>, Guoqiang Xu <sup>a,b,c</sup>, Xiuting Gu <sup>a,b,c</sup>, Jingshuai Yao <sup>a,d</sup>, Mowen Li <sup>d</sup>, Ming Lei <sup>d</sup>, Qun Chen <sup>e, \*\*</sup>, Yanchen Fu <sup>a,b,c,\*</sup>

<sup>a</sup> Research Institute of Aero-Engine, Beihang University, Beijing, 100191, China

<sup>b</sup> Tianmushan Laboratory, Hangzhou, 310023, China

<sup>c</sup> Collaborative Innovation Center for Advanced Aero-Engine, Beihang University, Beijing, 100191, China

<sup>d</sup> Beijing Power Machinery Institute, Beijing, 100074, China

<sup>e</sup> Key Laboratory for Thermal Science and Power Engineering of Ministry of Education, Department of Engineering Mechanics, Tsinghua University, Beijing, 100084, China

### ARTICLE INFO

Handling editor: Ruzhu Wang

**Keywords:**

Thermodynamic system

Thermal management

Experimental analysis

Aero engine

Energy flow model

### ABSTRACT

Efficient thermal management systems (TMS) are crucial for advanced aerospace vehicles to handle the increased thermal loads from engine combustion and aerodynamic heating. Aero-engine TMS are uniquely characterized by their high compactness, reliability, and stringent safety requirements. This study proposes a multilevel heat exchange system using endothermic hydrocarbon fuel, air, and high-pressure water. An experimental platform was constructed to analyze the effects of mass flow rates and inlet temperatures on the system's thermodynamic characteristics. Thermal management strategies were developed to optimize these parameters, significantly reducing thermal loads during high-speed flight and enhancing system efficiency and safety. Results indicate that variations in thermal energy input to a heat exchanger on one branch have a limited impact on another branch. The fuel mass flow rate can modulate the temperature of all working fluids in the system, but it also affects combustion characteristics. A transfer matrix-based system model with high accuracy was established, coupled with a genetic algorithm to achieve holistic identification of the heat exchanger heat transfer characteristics in practical applications, achieving a maximum parameter deviation of -4.79 %. The results contribute to optimizing TMS for aero engines, improving thermal stability, and enhancing energy utilization efficiency.

### Nomenclature

(continued)

<i>A</i>	heat transfer area of HEX [ $\text{m}^2$ ]
<i>a</i>	calculation coefficient, $a = 1/RG_h$
<i>b</i>	calculation coefficient, $b = 1/RG_c$
<i>c<sub>p</sub></i>	isobaric specific heat capacity [ $\text{J}/(\text{kg}\cdot\text{K})$ ]
<i>d</i>	hydraulic diameter [mm]
<i>f</i>	calculation coefficient, $f = (mc_p)_4/[(mc_p)_4 + (mc_p)_5]$
<i>G</i>	heat capacity flow rate
<i>h</i>	heat transfer coefficient [ $\text{W}/(\text{m}^2\cdot\text{K})$ ]
<i>K</i>	overall heat transfer coefficient [ $\text{W}/(\text{m}^2\cdot\text{K})$ ]
<i>KA</i>	thermal conductivity of HEX [W/K]
<i>m</i>	mass flow rate [ $\text{kg}/\text{s}$ ]
<i>P</i>	pressure [MPa]
<i>Q</i>	heat transfer rate [W]
<i>R</i>	inlet temperature difference-based thermal resistance [K/W]

(continued on next column)

<i>T</i>	temperature [ $^\circ\text{C}$ ]
$\Delta T_m$	logarithmic mean temperature difference [ $^\circ\text{C}$ ]
<b>Greek symbols</b>	
$\Delta$	Difference
$\xi$	Distribution ratio of water flow in system branches [%]
<b>Subscripts</b>	
1	HEX-1
2	HEX-2
3	HEX-3
a	air
c	cold fluid
cal	calculated data
exp	experimental data
f	fuel
h	hot fluid

(continued on next page)

\* Corresponding author. Research Institute of Aero-Engine, Beihang University, Beijing, 100191, China.

\*\* Corresponding author.

E-mail addresses: [chenqun@tsinghua.edu.cn](mailto:chenqun@tsinghua.edu.cn) (Q. Chen), [yanchenfu@buaa.edu.cn](mailto:yanchenfu@buaa.edu.cn) (Y. Fu).

(continued)

in	inlet notes
internal	internal notes
out	outlet notes
w	water
<b>Abbreviations</b>	
CCA	Cooled Cooling Air
GA	Genetic Algorithm
HEX	Heat Exchanger
LMTD	Logarithmic Mean Temperature Difference
PCHE	Printed Circuit Heat Exchanger
PTCC	Precooled Turbine Combined Cycle
SABRE	Synergistic Air-Breathing Rocket Engine
TMS	Thermal Management System

## 1. Introduction

The development of future advanced aerospace vehicles involves achieving low-energy flight capabilities across airspaces (0–30 km) and speed ranges (0–6 Ma) [1,2]. However, as the Mach number of flight increases, the combined effects of heat release from engine combustion and aerodynamic heating during flight significantly increase the thermal load on the vehicle, posing substantial safety risks to its stable operation [3–6]. When the Mach number of the aircraft reaches 6, under the combined effects of combustion heat release and aerodynamic heating, the central flow temperature in the combustion chamber can reach 2500 K, and the aero engine wall heat flux can reach 3 MW/m<sup>2</sup>, resulting in a substantial thermal load on the aero engine. Consequently, the development and establishment of an advanced and effective thermal management system (TMS) has become a necessary technical approach for the future development of advanced aerospace propulsion.

The concept of thermal management in aero engines is to conduct top-level planning and distribution of thermal energy among subsystems or components from a systemic perspective, achieving efficient conversion, transportation, and transfer of thermal energy while enhancing energy utilization efficiency under the premise of ensuring safe and reliable engine operation. Based on this concept, researchers have proposed various thermal management technologies for aviation engines [7].

One of the prevalent methods of thermal management is the direct heat exchange cooling technique, which involves using the engine's inherent working media (compressor bleed air, bypass air, bearing cavity cooling air, low-temperature fuel, etc.) to directly exchange heat with high-temperature heat sources through heat exchangers (HEXs) or cooling channels. The Precooled Turbine Combined Cycle (PTCC) engines primarily use hydrogen as fuel, typically stored in the liquid state, which has an extremely low temperature (boiling point at 0.1 MPa is 20.32 K) [8]. Therefore, a key technology in the TMS of the PTCC engines is the efficient utilization of the heat sink of liquid hydrogen. In the early development of PTCC engines, precoolers were typically installed before the compressor inlet, where liquid hydrogen and high-temperature air directly exchanged heat through the precooler, representatives including LACE [9–11], RB545 [12], and ATRDC [13, 14]. Cooled Cooling Air technology (CCA), proposed in the 1990s [15], is a representative example of direct heat exchange cooling technology in TMSs of aero engines [16]. CCA technology utilizes inlet ram air, bypass air, or fuel as coolants to effectively cool the compressor bleed air, addressing the growing demands for thermal protection [17]. The AL-31F engine represents a milestone in the development of CCA technology, being the first in-service engine to utilize this technique. It uses an air-air HEX installed in the bypass duct to precool the compressor bleed air for cooling high-temperature turbine guide vanes, achieving a cooling air temperature reduction of 125–210 K [18]. Moreover, both the US adaptive versatile engine technology project [19] and the Europe NEWAC project (New Aero Engine Core concepts) [20] adopt the CCA technology, improving the aero engine thermal efficiency through direct

heat exchange between compressor bleed air and bypass air. Nevertheless, increasing heat levels in future advanced aerospace vehicles have increased reliance on fuel as a coolant. The advantages of employing fuel as a heat sink in aero engines come from various factors such as higher heat sink [21], superior cooling capacity, closer to the cooling demand of the system, lighter CCA HEX [22], and so on. Duncan et al. [23] conducted experiments to explore the CCA technology effects on the external aerodynamics of combustion systems. Miller [24] analyzed a turbojet cycle that incorporated methane-air CCA technology versus a reference cycle, noting reductions of 1.2 % in specific thrust and 1 % in specific impulse. Boyle and Jones [25] noticed that cooling the turbine air before it enters the system significantly lowers specific fuel consumption. However, this cooling leads to a lower enthalpy in the air, which could lead to negative effects that outweigh the benefits of this precooling process. The impact of CCA technology on the aerothermal performances of aero engines with low bypass ratios was examined, with specific impacts noted across different flight altitudes and Mach numbers, as reported by Zhuang et al. [26].

The direct heat exchange cooling technology in TMS introduces only one additional component, a HEX, which has a minimal impact on the additional weight of the aero engine and offers high heat transfer efficiency. However, there are still many issues to be addressed in the practical application of this technology in aero engines. For PTCC engines or hydrogen-powered aircraft, employing direct heat exchange cooling technology to utilize the heat sink of liquid hydrogen presents several issues: (i) hydrogen embrittlement [27] can occur in the HEX, leading to a significant reduction in its structural strength, compromising its reliability in engine applications [28]. (ii) icing of the HEX. Frost control technology [29] is crucial for liquid hydrogen-air HEX. At flight altitudes below 12 km, direct heat exchange between liquid hydrogen and air rapidly cools the incoming air, causing rapid liquefaction and solidification of water vapor in the intake air, leading to frost formation on the external surfaces of heat exchange tubes, which not only deteriorates heat transfer performance but also blocks the air-side flow paths. (iii) safety risks. The HEX operates under complex alternating loads [30], posing a risk of heat exchange unit damage. Direct heat exchange between liquid hydrogen and high-temperature air can pose a fire risk if the heat exchange elements fail. For CCA technology, direct heat exchange between fuel and air carries safety risks as well. If the fuel-air HEX is damaged, leaking fuel into high-temperature air could cause the engine to catch fire. Besides, thermo-acoustic oscillations and fuel coking [31] posed considerable obstacles in the operation of the fuel-air HEXs, as noted by Herring and Heister [22].

Considering the drawbacks of direct heat exchange cooling technology in TMS, researchers proposed multilevel heat exchange systems with multifluid. In the early 1990s, Reaction Engines Limited initiated the Skylon project [32], innovatively proposing the Synergistic Air-Breathing Rocket Engine (SABRE) concept [33]. The core feature of the SABRE lies in its multilevel heat exchange system, which includes three types of HEXs: helium-air precooler, helium-gas HEX, and hydrogen-helium HEX [34]. Essentially, the cooling of ram air and high-temperature gas is still achieved using the heat sink of low-temperature liquid hydrogen. However, the introduction of helium as an intermediate working fluid in a closed cycle achieves the indirect transfer of heat. The multilevel heat exchange system with multifluid not only improves the thermal energy utilization efficiency of the engine but also effectively addresses issues such as hydrogen embrittlement and safety risks associated with precoolers. In the course of SABRE's development, it gradually evolved into the SABRE-3 [35], SABRE-4 [36], and Scimitar [2] designs, all of which also adopted multilevel heat exchange systems with multifluid. For scramjets, Dang et al. [37] compared the different layouts in the closed-Brayton-cycle-based segmented cooling TMS, and the closed-Brayton-cycle working fluid was employed as the intermediate working fluid to cool the engine wall and preheat the fuel. Cheng et al. [38] proposed a fuel indirect cooling-based TMS using liquid metal as the intermediate working fluid and evaluated its thermal

performance. Their results show that the proposed TMS has good combustion chamber wall protection performance. Besides, Zhang et al. [39] also studied the performance and feasibility of employing liquid metal to turbine guide vane cooling.

Multi-stage cooling technology may involve the use of an intermediate working fluid to develop a multilevel heat exchange system, thereby achieving efficient thermal energy utilization. Wang et al. [40] proposed a multi-stage precooling-compression cycle for PTCC engines and analyzed the system thermodynamic characteristics by numerical calculation. Zhang et al. [41] developed a two-stage expansion cooling system with exhaust air heat recovery and a subcooled liquid-to-air reheating coil for a dedicated outdoor air system in air-conditioning applications. The prototype test showed the system outperformed conventional cooling systems, exhibiting an efficiency increase of 26 %. Thermoelectric coolers often use multi-stage cooling technology [42]. A two-stage thermoelectric cooler system with respect to supercooling was proposed and optimized by Buchalik et al. [43,44]. Results showed that the developed system achieved momentary supercooling temperatures by about 18 K lower compared to the steady state. Yang et al. [45] designed a two-stage evaporative cooling system with composite activated carbon fiber dehumidification, aiming to reduce the air temperature below the ambient air wet bulb temperature. Overall, the limited space and weight constraints of aero engines restrict the extent of research into multi-stage cooling technology applications within these engines. Furthermore, employing the intermediate working fluid is not essential for multi-stage cooling systems. Consequently, further researches into intermediate heat exchange cycle systems within aero engines are necessary.

Recently, to further the implementation of CCA technology, studies have suggested the use of multilevel heat exchange systems with multifluid in turbofan engines. Fu et al. [46] proposed a thermodynamic model to optimize the heat transfer area of the intermediate heat exchange cycle system for aero engines. Liu et al. [47] developed a theoretical model of an intermediate heat exchange cycle system and conducted experiments to validate its accuracy. Results showed that the deviations between simulation results and experimental data were within  $\pm 10\%$ . The optimization of the aero-engine thermal management system with intermediate cycles based on an artificial neural network and heat current method was studied by Liu et al. [48,49]. However, in their experiments, they only used water to substitute for other working fluids like air, oil, and fuel, which deviates somewhat from the actual conditions in aero engines. Generally, research on multilevel heat exchange systems with multifluid is mostly restricted to system optimization analysis and numerical simulations. Experimental research on multilevel heat exchange systems with multifluid is limited, and the formulation of thermal management strategies for these systems lacks support from relevant experimental data. Therefore, the present research gap lies in experimental studies on the impact of different parameter variations on the thermodynamic characteristics of multilevel heat exchange systems, and formulating thermal management strategies based on experimental data analysis.

A highly efficient modeling method is essential for directly understanding and analyzing the thermodynamic characteristics of the multilevel heat exchange system with multifluid. Present modeling techniques are based on the physical analysis of individual components, stacking governing equations according to component layout to develop the mathematical model of the system [50]. In complex systems, however, these techniques involve numerous governing equations that necessitate iterative solutions due to their nonlinearity, significantly increasing computational time [51,52]. Expanding on the entransy theory [53], Chen et al. [54,55] introduced the heat current method, which facilitates the analysis and optimization of thermal systems through the use of thermo-electrical analogy and radiation-network method. Recently, in response to some shortcomings of the heat current method in practical applications, Chen et al. [56,57] have further proposed the transfer matrix-based method, which is mathematically

equivalent to the heat current method but easier to utilize since it does not require a topology transformation from fluid network to energy flow network or graphical modeling. Considering the various advantages of the transfer matrix-based method, the present study employs this method to establish the thermodynamic model of the multilevel heat exchange system with multifluid and validate the model's accuracy using experimental data.

This study establishes an experimental platform for a multilevel heat exchange system in an aero engine, coupling three HEXs serving different purposes and using endothermic hydrocarbon fuel, high-temperature air, and high-pressure water as working fluids. The research investigates the thermodynamic characteristics of the multilevel heat exchange system for aero engines, exploring the effects of variations in working fluids mass flow rates, inlet temperatures, and the distribution ratio of water flow in system branches on system characteristics. Based on experimental data, thermal management strategies have been developed. Finally, a theoretical model of the system is established using the transfer matrix-based method, and its accuracy is validated through experimental data. The model is further developed by coupling with the genetic algorithm to achieve holistic identification of the HEX heat transfer characteristics in practical applications.

## 2. Experimental facility

### 2.1. Experimental system

Based on the practical requirements of thermal management in aero engines, the current study designs and constructs a multilevel heat exchange system with multifluid. This system aims to utilize high-pressure water as an intermediate working fluid to simultaneously cool the compressor bleed air and bearing cavity cooling air and preheat the aviation kerosene. In the preliminary evaluations, other fluids such as helium, hexamethyldisiloxane, and thermal oil were considered for their potential as intermediate working fluids. However, after extensive assessments of safety, experimental operability, and hydraulic characteristics, high-pressure water was selected due to its accessibility, stability, and safety—qualities vital for experimental validation. It should be noted that using water as an intermediate working fluid is not the sole option. Depending on the specific application background and requirements of the aero engine, alternative fluids may be selected. Fig. 1(a) illustrates the principle of the system, which consists of three different types of HEXs, as shown in Fig. 1(b). HEX-1 is a compressor bleed air-water HEX utilizing a serpentine tube bundle design [58]. HEX-2 is a bearing cavity cooling air-water HEX with a typical shell and tube structure. HEX-3 is a fuel-water HEX, featuring a printed circuit heat exchanger (PCHE) with airfoil fins [59].

The test rig for the multilevel heat exchange system is shown in Fig. 2. The experimental setup constitutes five primary sub-systems: the compressor bleed air system, the bearing cavity cooling air system, the high-pressure water system, the fuel system, and the cooling water system. Chinese aviation kerosene RP-3 is used as fuel, and the water pressure is maintained above 2 MPa to avoid boiling, thereby ensuring the system's stability. As boiling water is typically concurrent with the formation of bubbles and turbulence, both of which can exert an influence on the hydraulic characteristics within the system. The only difference between the compressor bleed air system and the bearing cavity cooling air system is that they use different types of air heaters. Within the air pathway, an electric control valve and a Coriolis mass flowmeter are used to adjust and measure the air mass flow rate. Subsequently, an air heater is used to heat the air to a set temperature. Following this, the high-temperature air transfers heat to the water in HEX-1 and HEX-2 before being discharged directly into the surroundings. In the high-pressure water path, before the experiment, the water in the storage tank is pressurized to a predetermined level using high-pressure nitrogen. Subsequently, this high-pressure water is driven by a circulating pump and passes through a check valve to prevent any backflow. The

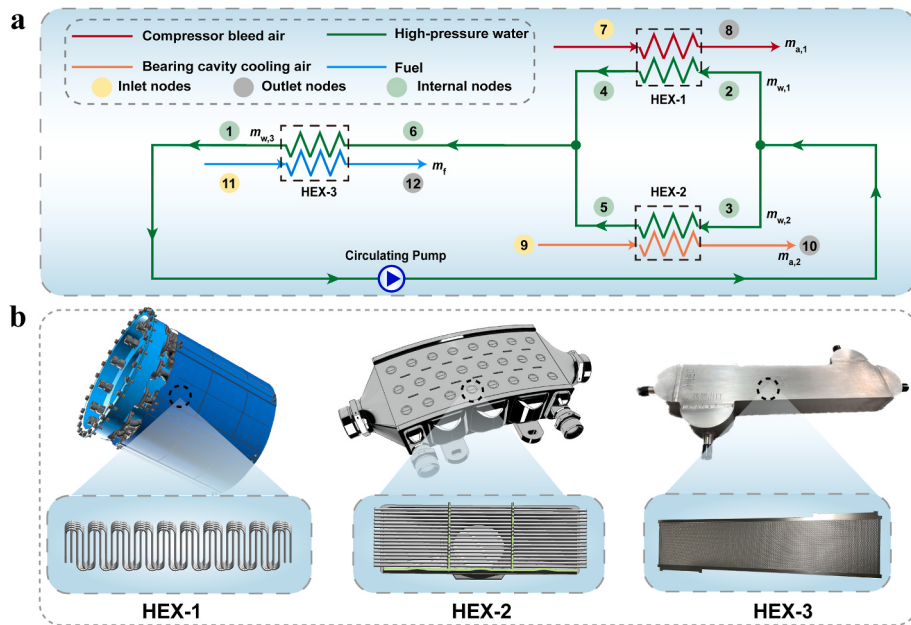


Fig. 1. Schematic diagram of the multilevel heat exchange system with multifluid. a: Schematic diagram of the system principle; b: Structure of HEXs.

high-pressure water flow path connects the three HEXs. HEX-1 and HEX-2 are located on parallel branches, while HEX-3 is situated on the main flow path. The mass flow rate of high-pressure water in the branch and main pathways is regulated by throttle valves and measured by Coriolis mass flowmeters. Along the fuel path, aviation kerosene RP-3, drawn from a storage tank at room temperature, is pressurized using a triple plunger pump. The fuel then flows through a Coriolis mass flowmeter before being heated by the high-pressure water in HEX-3. Subsequently, it is cooled in a double-pipe water cooler, which is the main component of the cooling water system, and the pressure of the fuel system is adjusted using a back-pressure valve. Finally, the fuel is returned to the RP-3 recycling tank.

K-type sheathed thermocouples are employed to measure temperatures at the inlet and outlet of each HEX. Fig. 3 depicts the placement of temperature and pressure sensors in different HEXs within the system. Thermocouples were placed at the inlet and outlet of the cold and hot sides of the HEX, approximately 7 cm away from the head of the HEX, to minimize the influence of external thermal disturbances. Specifically, HEX-1 is enclosed within an annular passage, with six identical heat exchange cores evenly distributed annularly. To accurately measure the average inlet and outlet temperatures of air within HEX-1, four thermocouples are placed in the same inlet cross-section and six thermocouples are placed in the same outlet cross-section. The bulk temperatures at both points are calculated using the mass flow averaging method. Rosemount absolute pressure transducers (Model 3051CA2, 3051CA4) and differential pressure transducers (Model 3051CD2) are employed to gauge pressure drops and absolute pressures along the fuel, compressor bleed air, bearing cavity cooling air, and high-pressure water paths. Pressure sensors are placed close to the temperature sensors. Data from these measurements are collected by multiple ADAM 4118 data acquisition modules, relayed through ADAM 4520, and finally interfaced with an Industrial Personal Computer. The ADAM 4118 module has a sampling frequency of 100 Hz. However, given that the current research primarily investigates the steady-state characteristics of the multilevel heat exchange system, this high data collection frequency is unnecessary. Consequently, we have adjusted the data collection frequency to 4 Hz. This adjustment was based on preliminary trials, which demonstrated that a 4 Hz frequency is sufficient to

capture all relevant system changes while ensuring the integrity of the data. To minimize heat loss during experiments, thermal insulation material covers all high-temperature pipelines and HEXs.

## 2.2. Data reduction

To ensure the collected data accurately reflected steady-state conditions, specific criteria based on the stability of temperature, pressure, and mass flow rate readings were established. The system was deemed to have reached a steady state when the variations in these parameters were less than 1 % over a 15-min period. Additionally, for data collection at a single operating point, four sets of data are recorded and collected within 20 s, and their average is calculated to represent the experimental data for that specific operating condition.

The thermodynamic characteristics of the multilevel heat exchange system are primarily indicated by the variations in heat transfer rates ( $Q$ ) of each HEX and temperature variations at various system nodes. The numbering of the system nodes is defined as shown in Fig. 1(a). The heat transfer rates of different working fluids across the HEX within the system are calculated by the following equations. Experimental results from the literature provide the density and isobaric specific heat capacity ( $c_p$ ) values for aviation kerosene RP-3 [60,61]. Thermal properties and associated uncertainties of water and air are obtained from the open-source CoolProp Library [62].

$$Q_{a,1} = m_{a,1} c_{p,a1} (T_7 - T_8) \quad (1)$$

$$Q_{w,1} = m_{w,1} c_{p,w1} (T_4 - T_2) \quad (2)$$

$$Q_{a,2} = m_{a,2} c_{p,a2} (T_9 - T_{10}) \quad (3)$$

$$Q_{w,2} = m_{w,2} c_{p,w2} (T_5 - T_3) \quad (4)$$

$$Q_{w,3} = m_{w,3} c_{p,w3} (T_6 - T_1) \quad (5)$$

$$Q_f = m_f c_{p,f} (T_{12} - T_{11}) \quad (6)$$

where subscripts “a”, “w”, and “f” respectively represent air, high-pressure water, and fuel; subscripts “1”, “2”, and “3” are HEX-1, HEX-

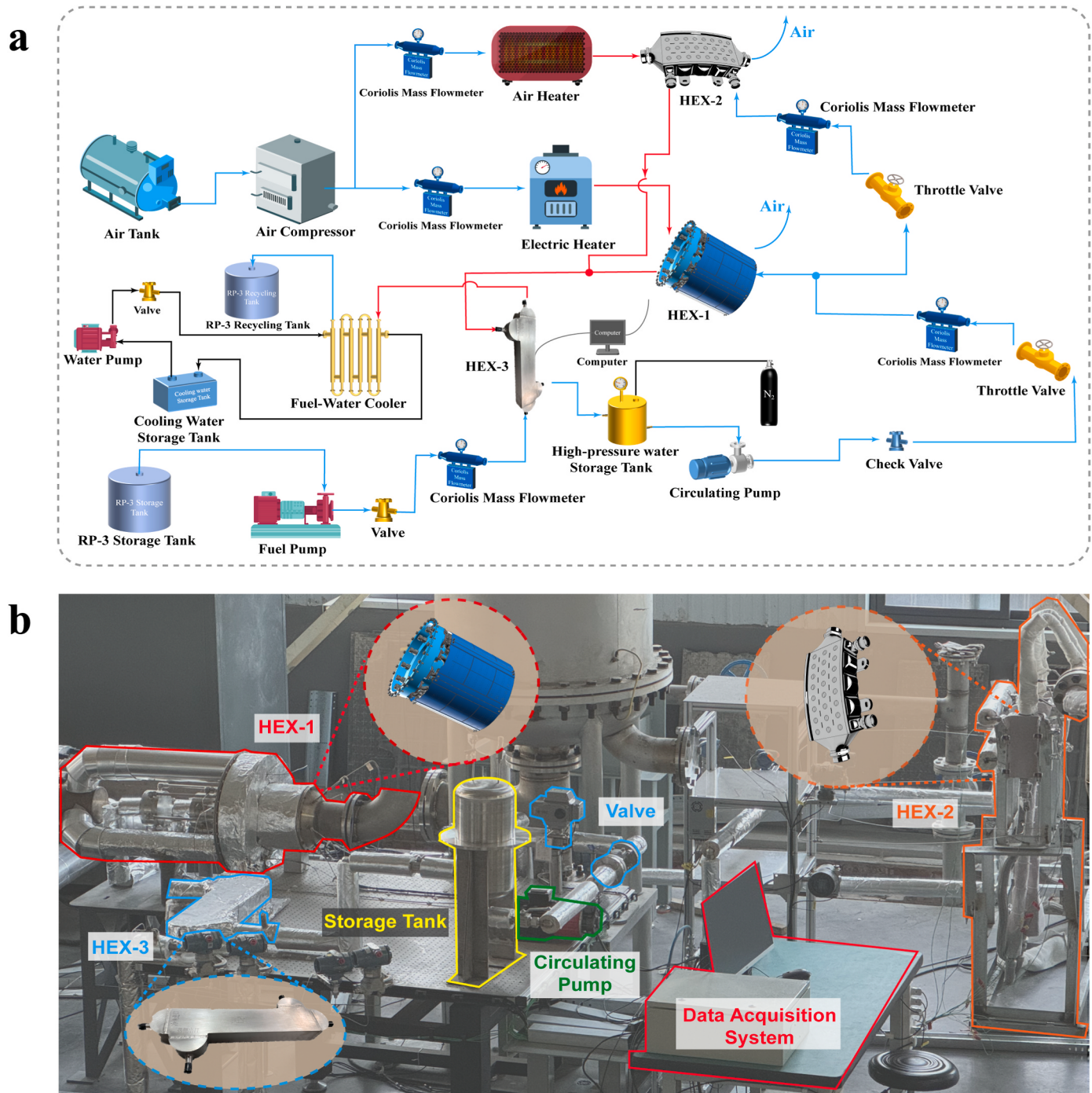


**Fig. 2.** Test rig for the multilevel heat exchange system with multifluid. a: Schematic diagram of the experimental system; b: A photograph of the experimental setup.

2, and HEX-3, respectively.

The average  $Q$  between the cold-side fluid and hot-side fluid of each HEX is expressed as below:

$$Q_1 = (Q_{a,1} + Q_{w,1}) / 2 \quad (7)$$

$$Q_2 = (Q_{a,2} + Q_{w,2}) / 2 \quad (8)$$

$$Q_3 = (Q_{w,3} + Q_f) / 2 \quad (9)$$

All HEXs in the system are set up in a counterflow configuration. The logarithmic mean temperature difference (LMTD) of each HEX is calculated as follows:

$$\Delta T_{m,1} = \frac{(T_7 - T_4) - (T_8 - T_2)}{\ln\left(\frac{T_7 - T_4}{T_8 - T_2}\right)} \quad (10)$$

$$\Delta T_{m,2} = \frac{(T_9 - T_5) - (T_{10} - T_3)}{\ln\left(\frac{T_9 - T_5}{T_{10} - T_3}\right)} \quad (11)$$

$$\Delta T_{m,3} = \frac{(T_6 - T_{12}) - (T_1 - T_{11})}{\ln\left(\frac{T_6 - T_{12}}{T_1 - T_{11}}\right)} \quad (12)$$

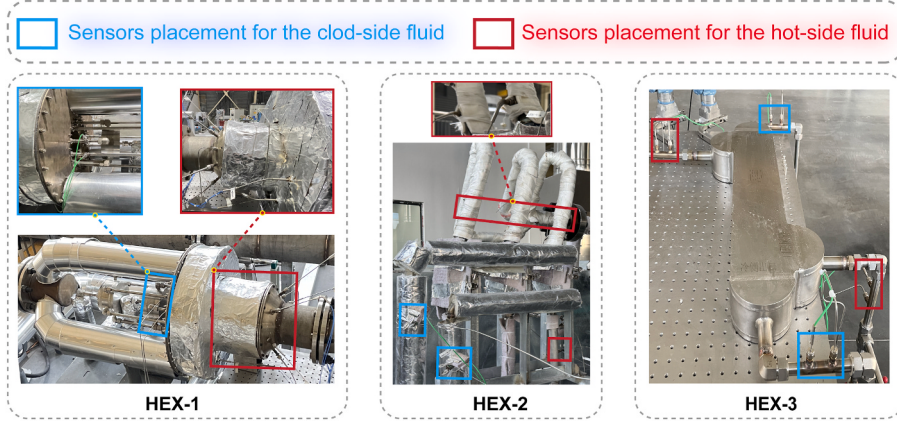


Fig. 3. Schematic diagram of the placement of temperature and pressure sensors in different HEXs within the system.

The thermal conductivity ( $KA$ ) of each HEX is calculated by the following equations.

$$KA_1 = \frac{Q_1}{\Delta T_{m,1}} \quad (13)$$

$$KA_2 = \frac{Q_2}{\Delta T_{m,2}} \quad (14)$$

$$KA_3 = \frac{Q_3}{\Delta T_{m,3}} \quad (15)$$

### 2.3. Uncertainty analysis

The working range and uncertainties of direct measurement for the test rig are detailed in Table 1. Utilizing the error propagation formula [63], for variables  $x_1, x_2, \dots, x_n$ , which are used in the computation of the variable ( $y$ ) based on Eq. (16). Assuming measurements with uncertainties  $\delta x_1, \delta x_2, \dots, \delta x_n$ , and uncertainties in  $x_1, x_2, \dots, x_n$  are random and independent, the uncertainty in  $y$  is determined as follows:

$$y = f(x_1, x_2, \dots, x_n) \quad (16)$$

Table 1  
Range and uncertainty of direct measurements.

Direct measurement	Measuring instrument	Range	Uncertainty
Fuel mass flow rate	Sincerity DMF-1-U15GWGY Coriolis Flowmeter	0–0.5 kg/s	±0.2 %
Air mass flow rate	Sincerity DMF-1-6AB Coriolis Flowmeter	0–0.5 kg/s	±0.5 %
Air mass flow rate	Sincerity DMF-1-6C Coriolis Flowmeter	0–1.0 kg/s	±0.5 %
Water mass flow rate	Endress + Hauser Promass E300 Coriolis Flowmeter	0–0.5 kg/s	±0.15 %
Water mass flow rate	Endress + Hauser Promass E300 Coriolis Flowmeter	0–0.3 kg/s	±0.15 %
Absolute pressure	Rosemount 3051CA4 pressure transmitter	0–10 MPa	±0.04 %
Absolute pressure	Rosemount 3051CA2 pressure transmitter	0–1 MPa	±0.04 %
Pressure drop	Rosemount 3051CD2 pressure transmitter	0–100 kPa	±0.04 %
Pressure drop	Rosemount 3051CD2 pressure transmitter	0–50 kPa	±0.04 %
Pressure drop	Rosemount 3051CD2 pressure transmitter	0–30 kPa	±0.04 %
Temperature	Kaipusen K-type sheathed thermocouple	223.15–1423.15 K	±1.5 K

Table 2  
The maximum uncertainties of heat transfer rates.

Parameters	Uncertainty	Parameters	Uncertainty
$Q_{a,1}$	3.49 %	$Q_{w,1}$	6.24 %
$Q_{a,2}$	2.36 %	$Q_{w,2}$	4.97 %
$Q_{w,3}$	4.56 %	$Q_f$	9.24 %
$Q_1$	3.58 %	$Q_2$	2.82 %
$Q_3$	5.11 %		

$$\delta y = \sqrt{\left(\frac{\partial y}{\partial x_1} \delta x_1\right)^2 + \left(\frac{\partial y}{\partial x_2} \delta x_2\right)^2 + \dots + \left(\frac{\partial y}{\partial x_n} \delta x_n\right)^2} \quad (17)$$

Combining the uncertainty of direct measurements, the calculated maximum relative uncertainties of  $Q$  for each HEX are listed in Table 2.

### 3. Experimental results and thermal management strategy discussions

To thoroughly explore the impact of various parameters on the thermodynamic characteristics of the multilevel heat exchange system with multifluid and to develop thermal management strategies based on this, the current study conducts multiple experiments, focusing on the effects of compressor bleed air mass flow rate ( $m_{a,1}$ ), bearing cavity cooling air mass flow rate ( $m_{a,2}$ ), fuel mass flow rate ( $m_f$ ), high-pressure water mass flow rate ( $m_{w,3}$ ), compressor bleed air inlet temperature ( $T_7$ ), and bearing cavity cooling air inlet temperature ( $T_9$ ) on the system's thermal performance. Detailed experimental data and boundary conditions are provided in Appendix A. Considering the actual application conditions of TMSs in aero engines, the system's thermal performance is primarily reflected in the variations of internal node temperatures, variations of outlet node temperatures, and changes in heat transfer rates of each HEX within the system. Thus, this research primarily examines how changes in various parameters affect these three types of parameters.

Fig. 4 illustrates the comparison of heat transfer rates between the hot and cold sides for each HEX within the system, revealing a relative deviation within 10 %, which confirms the reliability of the data gathered. For the multilevel heat exchange system with multifluid, the intermediate working fluid serves as the third fluid playing a role in the indirect transfer of thermal energy. Therefore, based on the configuration of the present system depicted in Fig. 1(a), theoretically, the heat exchanged between high-pressure water and the cold source fuel ( $Q_3$ ) should be equivalent to the sum of the heat exchanges between high-pressure water and the two high-temperature air sources ( $Q_1$  and  $Q_2$ ). Specifically, in the absence of heat losses,  $Q_3$  should be equal to  $(Q_1 + Q_2)$ . Fig. 5 shows the comparison between  $Q_3$  and  $(Q_1 + Q_2)$ , illustrating a

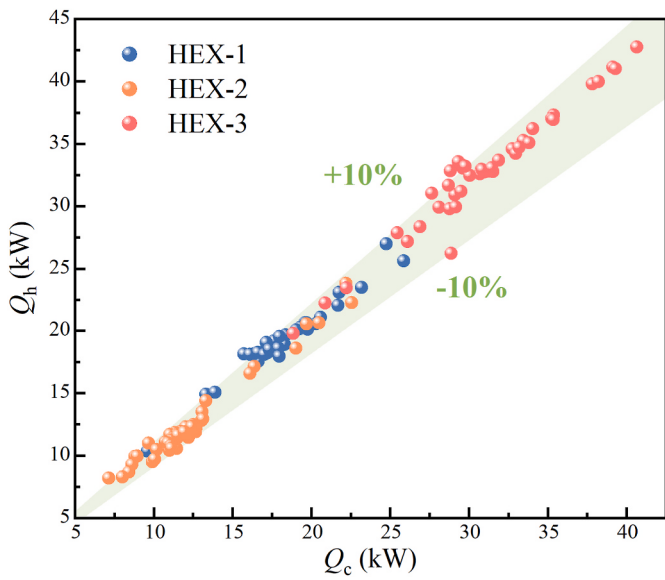


Fig. 4. Comparison of heat transfer rates between hot-side fluid and cold-side fluid of each HEX within the system.

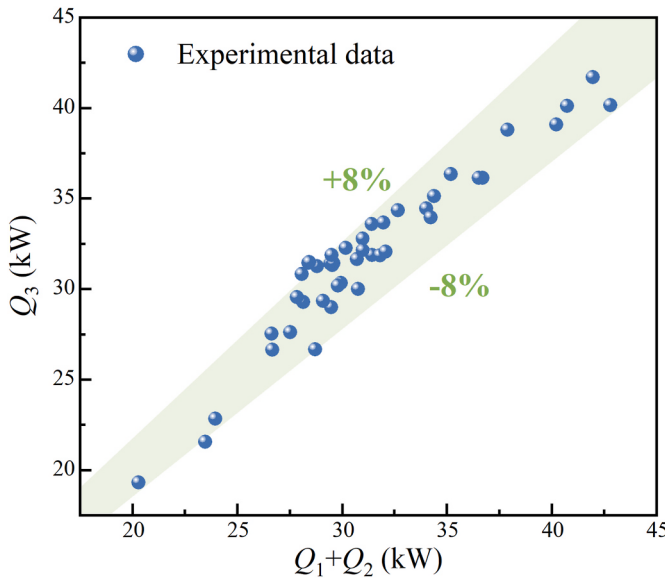


Fig. 5. Comparison between  $Q_3$  and  $(Q_1 + Q_2)$ .

relative deviation within 8 %, which demonstrates that heat losses are minimal during the experimental process and that the system has been stable when experimental data is collected.

### 3.1. Effect of the mass flow rate of compressor bleed air $m_{a,1}$

Experiments have been conducted with varying  $m_{a,1}$ . Table 3 indicates the detailed experimental conditions for the tests. Fig. 6(a) depicts the variations of internal node temperatures with  $m_{a,1}$ . Under the conditions of constant compressor bleed air inlet temperature, an increase in  $m_{a,1}$  results in a corresponding increase in the thermal energy input to the system. Observations show that  $T_1$ ,  $T_2$ , and  $T_3$  are basically equivalent, and they slightly rise with an increase in  $m_{a,1}$ . Since water flows from the main stream to the branches is a splitting process, theoretically, the temperatures at each node in this process should be equal. The experimental phenomenon shown in Fig. 6(a) corresponds with this theory, further validating the experimental data's reliability. In

Table 3

Experimental parameters for variable compressor bleed air mass flow rates.

Parameter	Value	Parameter	Value
$T_7$ (°C)	249.96	$m_{a,1}$ (kg/s)	0.160–0.300
$T_9$ (°C)	240.80	$m_{a,2}$ (kg/s)	0.069
$T_{11}$ (°C)	39.74	$m_{w,1}$ (kg/s)	0.062
$P_{a,1,in}$ (MPa)	0.103	$m_{w,2}$ (kg/s)	0.040
$P_{a,2,in}$ (MPa)	0.110	$m_{w,3}$ (kg/s)	0.102
$P_{f,in}$ (MPa)	2.951	$m_f$ (kg/s)	0.195
$P_{w,3,in}$ (MPa)	2.522		

HEX-1, compressor bleed air transfers heat with high-pressure water, so the water outlet temperature of HEX-1 ( $T_4$ ) increases with an increase in  $m_{a,1}$ . Besides,  $T_4$  exhibits an approximately linear relationship with  $m_{a,1}$ . However, it can be observed that as  $m_{a,1}$  increases,  $T_5$  does not change significantly but remains essentially constant. This indicates that in a multilevel heat exchange system, an increase in heat energy input to a HEX on one branch does not significantly affect the temperature of the intermediate working fluid on another branch. After the water from the two branches merges and flows into HEX-3,  $T_6$  also rises as  $T_4$  increases. Nevertheless, as can be seen from Fig. 6(a), anomalies are observed in the experimental results, with  $T_6$  occasionally exceeding both  $T_4$  and  $T_5$ , whereas theoretically,  $T_6$  should be between  $T_4$  and  $T_5$ . This discrepancy is primarily due to uneven heat exchange among the six identical heat exchange cores within HEX-1, as described in Section 2.1. Under the impact of uneven heat exchange, the measured  $T_4$  (representing the outlet temperature of water from one of the heat exchanger cores) might not reflect the average outlet temperature of all cores, thus occasionally resulting in temperatures lower than  $T_6$ .

The variations of outlet node temperatures are demonstrated in Fig. 6(b). As expected, the compressor bleed air outlet temperature ( $T_8$ ) increases with the increase in  $m_{a,1}$ . With the increase in  $T_6$ , the temperature difference for heat transfer in HEX-3 grows, causing water to transfer more heat to the fuel, thus increasing the fuel outlet temperature ( $T_{12}$ ). Similar to the previous phenomenon, although HEX-1 and HEX-2 are connected in parallel, changes in the heat input to HEX-1 do not significantly affect HEX-2, and  $T_{10}$  remains essentially unchanged as  $m_{a,1}$  increases.

Fig. 6(c) depicts the variations of the heat transfer rate of each HEX with  $m_{a,1}$ . The overall heat transfer coefficient ( $K$ ) of HEX-1 increases with the increase in  $m_{a,1}$ . Thus, the heat transfer capacity of HEX-1 grows, leading to the increase of  $Q_1$ . According to the aforementioned analysis, the effect of  $m_{a,1}$  on HEX-2 is limited. Consequently,  $Q_2$  remains basically constant. Combined with the changes in  $Q_1$  and  $Q_2$ ,  $Q_3$  correspondingly increases with the increase of  $m_{a,1}$ , since  $Q_3$  is equal to the sum of  $Q_1$  and  $Q_2$ . That is to say, the increase in compressor bleed air mass flow rate indirectly promotes the increase of heat sink transfer by the intermediate working fluid, and more heat is transferred to the fuel.

Based on the above thermodynamic characteristics, the thermal management strategies of the aero engine with a multilevel heat exchange system could be formulated. Increasing the compressor bleed air mass flow rate will lead to an increase in the thermal energy input to the multilevel heat exchange system, causing an increase in compressor bleed air outlet temperature, which is not conducive to the subsequent utilization of the compressor bleed air to cool the high-temperature turbine. Nevertheless, the impact of varying  $m_{a,1}$  on the bearing cavity cooling air-water HEX of the branch connected in parallel is quite limited. Therefore, when regulating the compressor bleed air mass flow rate in a multilevel heat exchange system, the main concern should be whether the bleed air outlet temperature meets aero-engine operating requirements, without overly focusing on the condition of the bearing cavity cooling air. Additionally, attention should be given to temperature  $T_4$ , which represents the highest water temperature within the entire system. It is crucial to prevent it from exceeding the boiling point, which could compromise the system's stability.

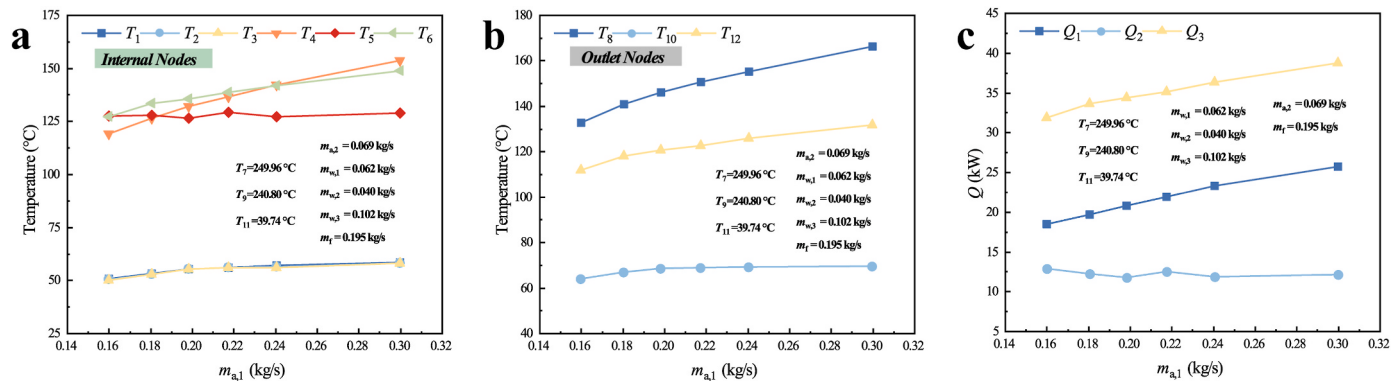


Fig. 6. The variation of different parameters with  $m_{a,1}$ . a: Internal node temperatures; b: Outlet node temperatures; c: Heat transfer rates of different HEXs.

Table 4  
Experimental parameters for variable bearing cavity cooling air mass flow rates.

Parameter	Value	Parameter	Value
$T_7$ (°C)	250.00	$m_{a,1}$ (kg/s)	0.196
$T_9$ (°C)	232.22	$m_{a,2}$ (kg/s)	0.070–0.214
$T_{11}$ (°C)	41.06	$m_{w,1}$ (kg/s)	0.059
$P_{a,1,in}$ (MPa)	0.102	$m_{w,2}$ (kg/s)	0.041
$P_{a,2,in}$ (MPa)	0.152	$m_{w,3}$ (kg/s)	0.100
$P_{f,in}$ (MPa)	3.063	$m_f$ (kg/s)	0.194
$P_{w,3,in}$ (MPa)	2.171		

### 3.2. Effect of the mass flow rate of bearing cavity cooling air $m_{a,2}$

Tests have been conducted with different  $m_{a,2}$  and the detailed experimental conditions are shown in Table 4. Since both HEX-1 and HEX-2 are located on the branches and involve air-water heat exchange, the effects of changes in bearing cavity cooling air and compressor bleed air mass flow rate on the multilevel heat exchange system follow the same patterns. Essentially, the differences are only in the source of the air, different air inlet parameters, and differences in the designs of HEXs. Hence, in the subsequent discussion, emphasis will be placed on describing the phenomena and thermal management strategies, rather than extensively analyzing the reasons for the changes. Fig. 7(a) demonstrates that the water outlet temperature of HEX-2 ( $T_5$ ) increases with an increase in  $m_{a,2}$ . And  $T_5$  is the highest water temperature for all internal nodes. Moreover, as  $m_{a,2}$  increases,  $T_4$  remains essentially constant, which again proves different branches have a certain independence. Combined with the variations of  $T_5$  and  $T_4$ ,  $T_6$  rises with the increase of  $m_{a,2}$ .

Fig. 7(b) illustrates the changes in outlet node temperatures with  $m_{a,2}$ . The bearing cavity cooling air outlet temperature ( $T_{10}$ ) rises as  $m_{a,2}$  increases. The fuel outlet temperature also increases with the increase in

$m_{a,2}$ . Nevertheless, the compressor bleed air outlet temperature remains relatively stable and is not significantly influenced by variations in  $m_{a,2}$ .

The variations of the heat transfer rate of each HEX with  $m_{a,2}$  are shown in Fig. 7(c). The increase in heat input to the bearing cavity cooling air leads to an increase in the heat transfer rate of HEX-2 ( $Q_2$ ). However,  $Q_1$  remains essentially unchanged, and as  $m_{a,2}$  continues to increase,  $Q_2$  eventually exceeds  $Q_1$ . Similar to the effect of compressor bleed air mass flow rate,  $Q_3$  increases with the increase of  $m_{a,2}$ .

Regarding the effect of bearing cavity cooling air mass flow rate, the resulting thermal management strategies of the aero engine with a multilevel heat exchange system are as follows. Increasing the bearing cavity cooling air mass flow rate will lead to an increase in water temperature and bearing cavity cooling air outlet temperature, which is not conducive to the subsequent utilization of the bearing cavity cooling air. However, increasing  $m_{a,2}$  has a quite limited influence on the thermal performance of compressor bleed air-water HEX. Based on this, when regulating the bearing cavity cooling air mass flow rate in a multilevel heat exchange system, the main concern should be on two items: the bearing cavity cooling air outlet temperature and internal node temperature  $T_5$ , which represents the highest water temperature within the entire system.

### 3.3. Effect of the mass flow rate of fuel $m_f$

Fig. 8 shows the variations of different parameters with fuel mass flow rate ( $m_f$ ) ranging from 0.083 kg/s to 0.250 kg/s. Table 5 illustrates the detailed experimental conditions for the tests. Fig. 8(a) plots the variations of internal node temperatures with  $m_f$ . Under the conditions of constant fuel inlet temperature, an increase in  $m_f$  results in a corresponding increase in the cold source within the system. Consequently, in HEX-3, where high-pressure water directly exchanges heat with fuel, the water outlet temperature ( $T_1$ ) will decrease with an increase in  $m_f$ . Since water flows from the main stream to the branches is a splitting process,

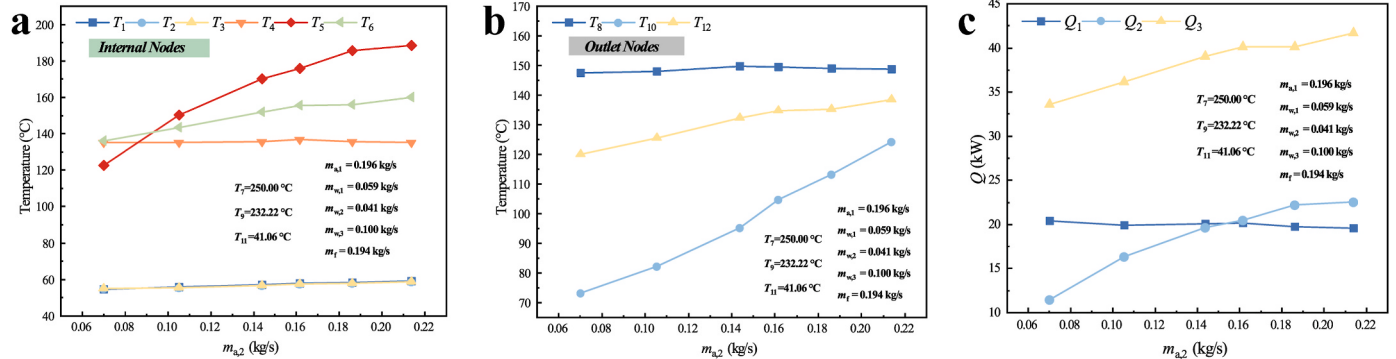


Fig. 7. The variation of different parameters with  $m_{a,2}$ . a: Internal node temperatures; b: Outlet node temperatures; c: Heat transfer rates of different HEXs.

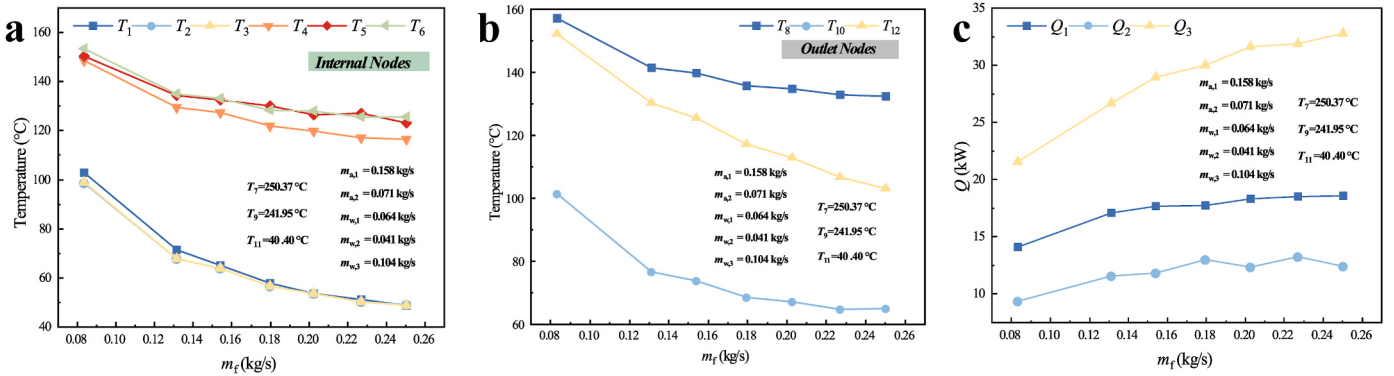


Fig. 8. The variation of different parameters with  $m_f$ . a: Internal node temperatures; b: Outlet node temperatures; c: Heat transfer rates of different HEXs.

**Table 5**  
Experimental parameters for variable fuel mass flow rate.

Parameter	Value	Parameter	Value
$T_7$ (°C)	250.37	$m_{a,1}$ (kg/s)	0.158
$T_9$ (°C)	241.95	$m_{a,2}$ (kg/s)	0.071
$T_{11}$ (°C)	40.40	$m_{w,1}$ (kg/s)	0.064
$P_{a,1,\text{in}}$ (MPa)	0.101	$m_{w,2}$ (kg/s)	0.041
$P_{a,2,\text{in}}$ (MPa)	0.111	$m_{w,3}$ (kg/s)	0.104
$P_{f,\text{in}}$ (MPa)	2.998	$m_f$ (kg/s)	0.083–0.250
$P_{w,3,\text{in}}$ (MPa)	2.645		

theoretically,  $T_1$ ,  $T_2$ , and  $T_3$  are equivalent, showing the same trend. For HEX-1 and HEX-2, as  $m_f$  increases, the inlet temperatures of the cold-side working fluids decrease, and consequently, the outlet temperatures of these cold-side working fluids ( $T_4$  and  $T_5$ ) also decrease. As for temperature  $T_6$ , water flows from the branches to the main stream is a mixing process, thus  $T_6$  decreases with the decrease of  $T_4$  and  $T_5$ . The changes in outlet node temperatures with  $m_f$  are shown in Fig. 8(b). For HEXs within the system, the water-side temperatures all decrease as  $m_f$  rises, consequently, the outlet temperature of the other-side fluid ( $T_8$ ,  $T_{10}$ , and  $T_{12}$ ) will decrease accordingly. As for the variation of the heat transfer rates of different HEXs depicted in Fig. 8(c), with an increase in  $m_f$ , the  $K$  of HEX-3 rises, enhancing the heat transfer and thus increasing  $Q_3$ . As analyzed earlier, the heat transfer temperature difference in HEX-1 and HEX-2 increases, which causes  $Q_1$  and  $Q_2$  to exhibit a rising trend.

The thermal management strategy developed in response to the variations in fuel mass flow rate is outlined below. Firstly, reducing the temperatures of the intermediate working medium, compressor bleed air, or bearing cavity cooling air within the system can be achieved by increasing the fuel mass flow rate. This approach aids in maintaining the thermal stability of the system and improving the engine's thermal efficiency. Secondly, by increasing  $m_f$ , the fuel outlet temperature could be decreased, ensuring it remains below the maximum allowable temperature. However, increasing the  $m_f$  will raise the fuel-to-air ratio in the combustion chamber of the aero engine, affecting the combustion characteristics. Therefore, the regulation of fuel mass flow rate should be coupled with considerations of the combustion requirements.

**Table 6**  
Experimental parameters for variable main stream water mass flow rates.

Parameter	Value	Parameter	Value
$T_7$ (°C)	250.47	$m_{a,1}$ (kg/s)	0.160
$T_9$ (°C)	237.65	$m_{a,2}$ (kg/s)	0.070
$T_{11}$ (°C)	39.27	$m_{w,1}$ (kg/s)	0.045–0.221
$P_{a,1,\text{in}}$ (MPa)	0.101	$m_{w,2}$ (kg/s)	0.030–0.144
$P_{a,2,\text{in}}$ (MPa)	0.111	$m_{w,3}$ (kg/s)	0.075–0.365
$P_{f,\text{in}}$ (MPa)	3.070	$m_f$ (kg/s)	0.195
$P_{w,3,\text{in}}$ (MPa)	2.324		

#### 3.4. Effect of the mass flow rate of main stream water $m_{w,3}$

Experiments have been conducted with varying main stream water mass flow rates ( $m_{w,3}$ ), and the experimental conditions are depicted in Table 6. The changes in internal node temperatures with  $m_{w,3}$  are shown in Fig. 9(a). In HEX-3, with high-pressure water acting as the hot-side working fluid, an increase in its mass flow rate indicates a larger heat source, thereby resulting in a higher water outlet temperature ( $T_1$ ) from HEX-3. Subsequently,  $T_2$  and  $T_3$  also increase as  $T_1$  increases. For HEX-2 and HEX-3, where high-pressure water serves as the cold-side working fluid, an increase in  $m_{w,3}$  also implies an increase in the water mass flow rate in each branch. Consequently, as the total amount of cold source in each branch increases, this results in a decrease in the water outlet temperatures ( $T_4$  and  $T_5$ ), subsequently causing the temperature  $T_6$  to drop.

As previously mentioned, the intermediate working fluid in a multilevel heat exchange system only serves to indirectly transfer thermal energy. Therefore, changing the main stream water mass flow rate only alters the thermal energy transfer rate and the temperatures at the internal nodes, without affecting the heat transfer rates of the system. Thus,  $Q_1$ ,  $Q_2$ , and  $Q_3$  do not vary with changes in  $m_{w,3}$ , as illustrated in Fig. 9(c). Based on Eqs. (2), (4) and (5), since the water mass flow rate increases and  $Q$  remains unchanged, the temperature difference between the inlet and outlet water in each HEX will decrease, which is consistent with the phenomenon shown in Fig. 9(a). The variations in outlet node temperatures are demonstrated in Fig. 9(b). Due to the constant heat transfer rate, mass flow rate, and inlet temperature of compressor bleed air, bearing cavity cooling air, and fuel, the outlet temperatures of these working media will not vary with  $m_{w,3}$ . However, it can be seen that  $T_{10}$  exhibits significant fluctuations with increases in  $m_{w,3}$ , with fluctuations exceeding 10 °C. This phenomenon is attributed to the variability in the inlet temperature of the bearing cavity cooling air ( $T_9$ ), which is not maintained at a constant value due to the operational characteristics of the air heater used in the experiments. Detailed data in Appendix A.2 shows that during the experiments investigating the effects of  $m_{w,3}$ ,  $T_9$  varied between 224.94 °C and 247.07 °C. This variation directly impacted  $T_{10}$ , leading to the observed fluctuations with the increase in  $m_{w,3}$ .

In the practical application of the multilevel heat exchange system with multifluid for aero engines, it is crucial to ensure the stability of the system. Preventing the intermediate working fluid from boiling is particularly important, as boiling water is often accompanied by the formation of bubbles and turbulence, which may result in shocks and vibrations to components. Based on the above analysis regarding the effect of  $m_{w,3}$ , adjusting the main stream water mass flow rate could change the internal node temperatures without influencing the thermal performance of the system. By increasing  $m_{w,3}$ , the maximum water temperature in the system can be lowered. However, it is important to note that the temperatures at internal nodes  $T_1$ – $T_3$  will rise, potentially

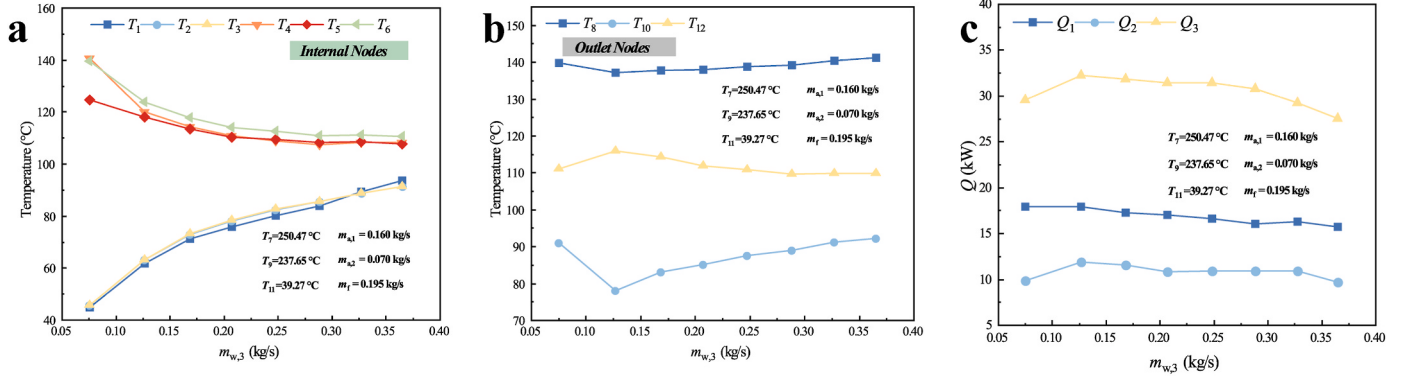


Fig. 9. The variation of different parameters with  $m_{w,3}$ . a: Internal node temperatures; b: Outlet node temperatures; c: Heat transfer rates of different HEXs.

impacting the ancillary components within the system.

### 3.5. Effect of air inlet temperatures $T_7$ and $T_9$

Fig. 10 demonstrates the variations of different parameters with compressor bleed air inlet temperature ( $T_7$ ) ranging from 150.22 °C to 350.43 °C. Table 7 indicates the detailed experimental conditions for the tests. Raising  $T_7$  means an increase in the heat input to the system, and it can be anticipated that this will raise the temperatures at different nodes within the system. As shown in Fig. 10(a) and (b), the internal node temperatures and outlet node temperatures all increase with an increase of  $T_7$ . Moreover, except for  $T_5$ , the increase in temperatures at various nodes generally exhibits a linear trend, which is consistent with the theoretical derivations in Ref. [47].  $T_5$  is the outlet temperature of the intermediate working fluid on another branch and observations show that  $T_5$  does not change significantly but remains essentially constant. It aligns with the findings in Sections 3.1 and 3.2, which state that in multilevel heat exchange systems, changes in the heat input of a HEX on one branch have a very limited impact on another branch. As for the heat transfer rate variations of each HEX depicted in Fig. 10(c), as  $T_7$  increases, the heat transfer temperature differences in HEX-1 and HEX-3 grow, resulting in an increase in  $Q_1$  and  $Q_3$ . In the case of HEX-2, since the mass flow rate and inlet temperature of the bearing cavity cooling air remain constant, the outlet temperature increases slowly, causing  $Q_2$  to gradually decrease.

The changes of different parameters with bearing cavity cooling air inlet temperature ( $T_9$ ) ranging from 183.75 °C to 419.81 °C are illustrated in Fig. 11. Similar to the effect of  $T_7$ , except for  $T_4$ , the temperatures at various nodes within the system increase with the rise in  $T_9$  and roughly follow a linear trend. Since HEX-1 is located on another branch,  $T_4$  remains essentially unchanged. Additionally, as the compressor bleed air outlet temperature slowly increases and  $m_{a,1}$  and  $T_7$  remain

Table 7

Experimental parameters for variable air inlet temperatures.

Parameter	Value	Parameter	Value
$T_7$ (°C)	150.22–350.43	$m_{a,1}$ (kg/s)	0.160
$T_9$ (°C)	183.75–419.81	$m_{a,2}$ (kg/s)	0.061
$T_{11}$ (°C)	41.15, 42.75	$m_{w,1}$ (kg/s)	0.061, 0.062
$P_{a,1,in}$ (MPa)	0.101	$m_{w,2}$ (kg/s)	0.039, 0.040
$P_{a,2,in}$ (MPa)	0.108	$m_{w,3}$ (kg/s)	0.100, 0.102
$P_{f,in}$ (MPa)	2.574	$m_f$ (kg/s)	0.235
$P_{w,3,in}$ (MPa)	3.000		

unchanged, the  $Q_1$  gradually decreases with the increase of  $T_9$ , while both  $Q_2$  and  $Q_3$  increase with  $T_9$ .

Given the above characteristics, for thermal management strategies of aero engines, increasing the pressure ratio, lowering the flight altitude, or increasing the flight Mach number, could increase the compressor bleed air inlet temperature ( $T_7$ ) and bearing cavity cooling air inlet temperature ( $T_9$ ). This enhancement allows the multilevel heat exchange system to absorb more heat, consequently increasing the temperature at various nodes within the system. Therefore, monitoring the fuel outlet temperature  $T_{12}$  and the highest water temperature ( $T_4$  or  $T_5$ ), ensuring they remain below the maximum allowable temperature, is particularly important.

### 3.6. Effect of the distribution ratio of water flow in branches $\xi$

The multilevel heat exchange system with multifluid is composed of several HEXs arranged in parallel and series, forming multiple branches. The current research investigates the effects of different branch intermediate working fluid flow ratios on the system's thermodynamic characteristics. Herein, the distribution ratio of water flow in system branches ( $\xi$ ) is defined as the proportion of the water mass flow rate in

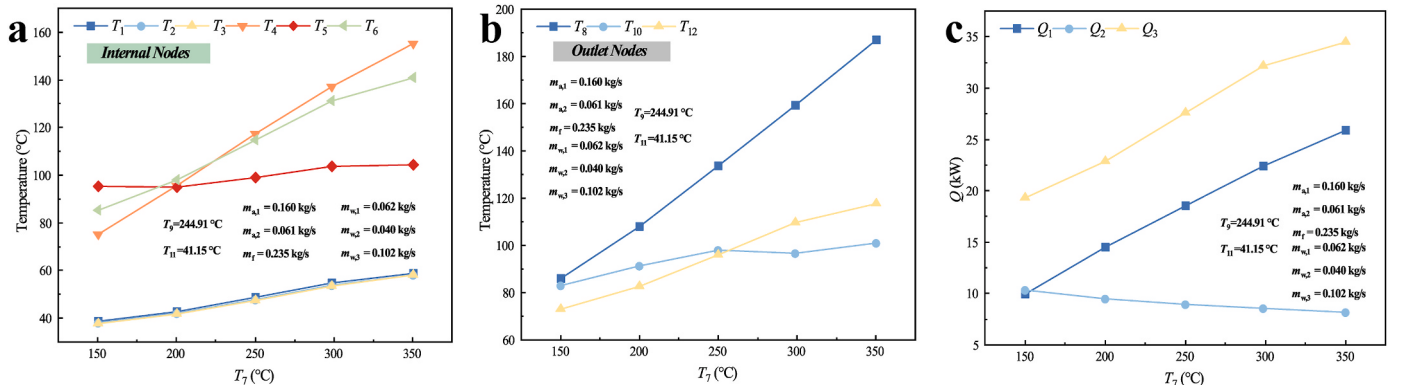
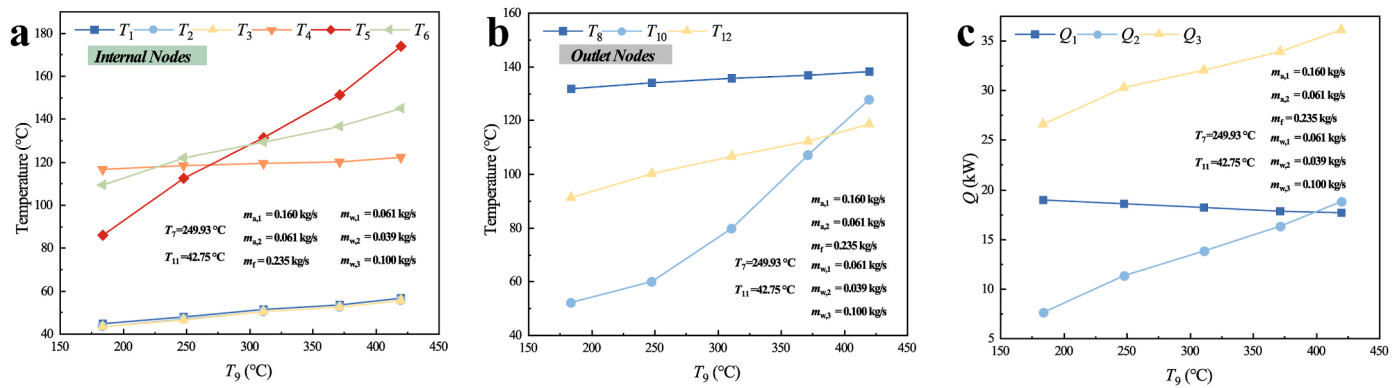


Fig. 10. The variation of different parameters with  $T_7$ . a: Internal node temperatures; b: Outlet node temperatures; c: Heat transfer rates of different HEXs.



**Fig. 11.** The variation of different parameters with  $T_9$ . a: Internal node temperatures; b: Outlet node temperatures; c: Heat transfer rates of different HEXs.

HEX-1 ( $m_{w,1}$ ) to the main stream water mass flow rate ( $m_{w,3}$ ), as shown in Eq. (18). Accordingly, the proportion of the water mass flow rate in HEX-2 ( $m_{w,2}$ ) to the main stream water mass flow rate ( $m_{w,3}$ ) is  $(1-\xi)$ .

$$\xi = \frac{m_{w,1}}{m_{w,3}} \times 100\% \quad (18)$$

In the case of constant main stream water mass flow rate  $m_{w,3}$ , Fig. 12 shows the variations of different parameters with  $\xi$  ranging from 59.83 % to 89.73 %. Table 8 shows the detailed experimental conditions for the tests. The changes in internal node temperatures with  $\xi$  are depicted in Fig. 12(a). As  $\xi$  increases,  $T_1-T_3$  remains essentially unchanged,  $T_4$  shows a slight decrease, while  $T_5$  significantly increases. It contributes to the fact that an increase in  $\xi$  means an increase in water mass flow rate in HEX-1 and a decrease in HEX-2, where water acts as the cold-side fluid in both HEXs. Therefore, as  $\xi$  increases, the cooling capacity of water in HEX-1 is enhanced, leading to a decrease in water outlet temperature ( $T_4$ ), while a decrease in  $m_{w,2}$  weakens the cooling capacity in HEX-2, causing the water outlet temperature ( $T_5$ ) to rise. Although  $T_5$  significantly increases, the mixed temperature  $T_6$  of the branch water remains largely unchanged. This is because  $T_6$  depends not just on the inlet temperatures of the branch flows, but also on their mass flow rates and the isobaric specific heat capacity. As for the outlet node temperature demonstrated in Fig. 12(b), due to the decrease in the cooling capacity of water in HEX-2, the bearing cavity cooling air outlet temperature ( $T_{10}$ ) increases, while  $T_8$  and  $T_{12}$  show only minor changes. Regarding the variations in heat transfer rate of the three HEXs shown in Fig. 12(c), the high-pressure water in the system only serves to indirectly transfer thermal energy. Thus,  $Q_3$  essentially does not vary with  $\xi$ .  $Q_1$  and  $Q_2$  undergo slight changes with variations in  $\xi$ , but their sum theoretically remains constant.

The thermal management strategies developed in response to the variations in the distribution ratio of water flow in system branches ( $\xi$ ) are outlined below. Modifying  $\xi$  enables the regulation of heat exchange

**Table 8**

Experimental parameters for variable distribution ratio of water flow in branches.

Parameter	Value	Parameter	Value
$T_7$ (°C)	250.76	$m_{a,1}$ (kg/s)	0.162
$T_9$ (°C)	243.04	$m_{a,2}$ (kg/s)	0.069
$T_{11}$ (°C)	39.83	$m_{w,3}$ (kg/s)	0.200
$P_{a,1,in}$ (MPa)	0.101	$m_t$ (kg/s)	0.195
$P_{a,2,in}$ (MPa)	0.111	$\xi$ (%)	59.83–89.73
$P_{t,in}$ (MPa)	2.907	$P_{w,3,in}$ (MPa)	2.369

in the system's branch HEXs without affecting the systematic thermal performance. For instance, increasing  $\xi$  could strengthen the heat transfer in HEX-1 and further reduce the compressor bleed air outlet temperature. Conversely, decreasing  $\xi$  can be employed to further lower the bearing cavity cooling air outlet temperature. Nonetheless, caution is required as extreme values of  $\xi$  could result in overly high temperatures at internal nodes, potentially exceeding the boiling point and compromising system stability. Specifically, a very high  $\xi$  can cause a sharp increase in temperature  $T_5$ , while a very low  $\xi$  can lead to a sharp increase in temperature  $T_4$ . Most importantly, the results indicate that adjusting the mass flow rate of the intermediate working fluid can change the temperature at various nodes within the system, thereby achieving regulation of heat sink distribution. This represents a significant improvement over traditional aero-engine TMSs.

In the actual operation of multilevel heat exchange systems, mismatches between preheating and cooling demands can pose safety risks and impact operational efficiency. To address these issues, responses are categorized based on the system's operating states:

**Steady-State Operations:** In steady-state conditions, a thorough initial design phase is crucial. Designers must carefully plan thermal management to accommodate various flight conditions, incorporating

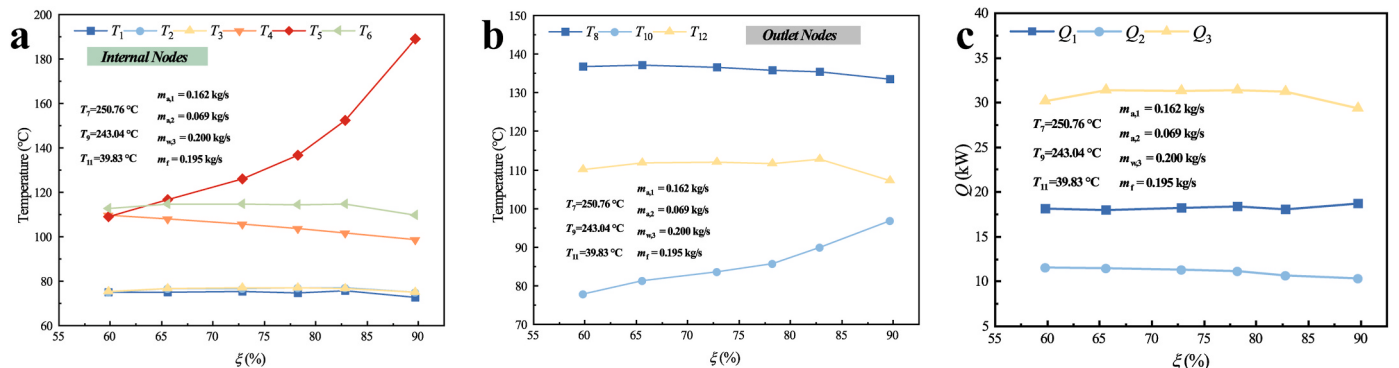


**Fig. 12.** The variation of different parameters with  $\xi$ . a: Internal node temperatures; b: Outlet node temperatures; c: Heat transfer rates of different HEXs.

precise thermal matching calculations. These calculations determine the appropriate mass flow rates and circulating temperatures of the intermediate working fluid. Such meticulous planning allows the system to fine-tune predefined operating parameters to meet the thermal energy demands during steady flight conditions, thus enhancing both efficiency and safety.

**Transient Processes:** Transient processes involve variations in engine operating conditions where thermal demand mismatches are more likely. Addressing these challenges requires the development of robust thermal management strategies and rapid adjustments of control components. This study establishes a foundation by analyzing the thermodynamic characteristics of the system under varying conditions and developing a high-precision system model. From this basis, designers can devise thermal control strategies to adapt to operational changes. Subsequently, control algorithms can be developed to facilitate swift adjustments.

#### 4. Transfer matrix-based system modeling

A highly efficient modeling method is essential for directly understanding and analyzing the thermodynamic characteristics of the multilevel heat exchange system with multifluid. This study utilizes the transfer matrix-based method to establish the system's thermodynamic model. To simplify the model, the following assumptions are applied:

1. Heat losses in pipelines and HEXs are ignored, and the heat transfer process only occurs between hot and cold fluids;
2. The multilevel heat exchange system operates at steady conditions;
3. The thermal properties of working fluids are constant, depending on their average temperature and pressure.

##### 4.1. Transfer matrix-based multilevel heat exchange system modeling

The transfer matrix-based method, proposed by Chen et al. [56,57], is mathematically equivalent to the heat current method but offers greater usability as it does not necessitate topology transformations from fluid networks to energy flow networks or graphical modeling. The transfer matrix-based method and heat current method have been successfully applied in many fields, including district heating systems [56], absorption energy storage systems [64], thermal power conversion in large-scale systems [65], liquid desiccant dehumidification process [66], Organic Rankine cycle systems, and so forth.

To keep this manuscript concise, only the main calculation and modeling processes are outlined below. For a detailed derivation process, please refer to Ref. [57].

The inlet temperature difference-based thermal resistance of counter-flow HEX is defined as [54]:

$$R = \frac{G_c \exp\left(\frac{KA}{G_h}\right) - G_h \exp\left(\frac{KA}{G_c}\right)}{G_h G_c \left[ \exp\left(\frac{KA}{G_h}\right) - \exp\left(\frac{KA}{G_c}\right) \right]} \quad (19)$$

where  $G$  represents the fluid heat capacity flow rate, i.e., the product of isobaric specific heat capacity and mass flow rate.

For the multilevel heat exchange system with multifluid illustrated in Fig. 1(a), the vector of node temperatures  $\mathbf{T}$  is expressed by:

$$\mathbf{T} = [T_1 \ T_2 \ T_3 \ T_4 \ T_5 \ T_6 \ T_7 \ T_8 \ T_9 \ T_{10} \ T_{11} \ T_{12}]^\top \quad (20)$$

The system-level transfer matrix equation [57] is:

$$\mathbf{H}_l \mathbf{T} = \mathbf{H}_r \mathbf{T} \quad (21)$$

The two coefficient matrices in Eq. (21) are expressed as:

$$\mathbf{H}_l = \begin{pmatrix} 1 & 0 & 0 & 0 & 0 & 0 & 0 & 0 & 0 & 0 & 0 & 0 \\ 0 & 1 & 0 & 0 & 0 & 0 & 0 & 0 & 0 & 0 & 0 & 0 \\ 0 & 0 & 1 & 0 & 0 & 0 & 0 & 0 & 0 & 0 & 0 & 0 \\ 0 & 0 & 0 & 1 & 0 & 0 & 0 & 0 & 0 & 0 & 0 & 0 \\ 0 & 0 & 0 & 0 & 1 & 0 & 0 & 0 & 0 & 0 & 0 & 0 \\ 0 & 0 & 0 & 0 & 0 & 1 & 0 & 0 & 0 & 0 & 0 & 0 \\ 0 & 0 & 0 & 0 & 0 & 0 & 1 & 0 & 0 & 0 & 0 & 0 \\ 0 & 0 & 0 & 0 & 0 & 0 & 0 & 1 & 0 & 0 & 0 & 0 \\ 0 & 0 & 0 & 0 & 0 & 0 & 0 & 0 & 1 & 0 & 0 & 0 \\ 0 & 0 & 0 & 0 & 0 & 0 & 0 & 0 & 0 & 1 & 0 & 0 \\ 0 & 0 & 0 & 0 & 0 & 0 & 0 & 0 & 0 & 0 & 1 & 0 \\ 0 & 0 & 0 & 0 & 0 & 0 & 0 & 0 & 0 & 0 & 0 & 1 \end{pmatrix} \quad (22)$$

$$\mathbf{H}_r = \begin{pmatrix} 0 & 0 & 0 & 0 & 0 & 1-a_3 & 0 & 0 & 0 & 0 & a_3 & 0 \\ 1 & 0 & 0 & 0 & 0 & 0 & 0 & 0 & 0 & 0 & 0 & 0 \\ 1 & 0 & 0 & 0 & 0 & 0 & 0 & 0 & 0 & 0 & 0 & 0 \\ 0 & 1-b_1 & 0 & 0 & 0 & 0 & b_1 & 0 & 0 & 0 & 0 & 0 \\ 0 & 0 & 1-b_2 & 0 & 0 & 0 & 0 & 0 & b_2 & 0 & 0 & 0 \\ 0 & 0 & 0 & f & 1-f & 0 & 0 & 0 & 0 & 0 & 0 & 0 \\ 0 & 0 & 0 & 0 & 0 & 0 & 0 & 0 & 0 & 0 & 0 & 0 \\ 0 & a_1 & 0 & 0 & 0 & 0 & 1-a_1 & 0 & 0 & 0 & 0 & 0 \\ 0 & 0 & 0 & 0 & 0 & 0 & 0 & 0 & 0 & 0 & 0 & 0 \\ 0 & 0 & a_2 & 0 & 0 & 0 & 0 & 0 & 0 & 1-a_2 & 0 & 0 \\ 0 & 0 & 0 & 0 & 0 & 0 & 0 & 0 & 0 & 0 & 0 & 0 \\ 0 & 0 & 0 & 0 & 0 & b_3 & 0 & 0 & 0 & 0 & 0 & 1-b_3 \end{pmatrix} \quad (23)$$

where set  $f = (mc_p)_4/[(mc_p)_4 + (mc_p)_5]$ , and the expressions for  $a_1$ ,  $a_2$ ,  $a_3$ ,  $b_1$ ,  $b_2$ , and  $b_3$  are given below:

$$\begin{cases} a_i = \frac{1}{(RG_h)_i}, & i = 1, 2, 3 \\ b_i = \frac{1}{(RG_c)_i} \end{cases} \quad (24)$$

In Eq. (24), the subscripts 1, 2, and 3 correspond to HEX-1, HEX-2, and HEX-3, respectively; 'h' represents the hot fluid, and 'c' represents the cold fluid.

Remove the redundant rows and columns in Eq. (21), the simplified system-level transfer matrix equation can be obtained:

$$\begin{pmatrix} T_1 \\ T_2 \\ T_3 \\ T_4 \\ T_5 \\ T_6 \\ T_8 \\ T_{10} \\ T_{12} \end{pmatrix} = \begin{pmatrix} 0 & 0 & 0 & 0 & 0 & 1-a_3 & 0 & 0 & a_3 \\ 1 & 0 & 0 & 0 & 0 & 0 & 0 & 0 & 0 \\ 1 & 0 & 0 & 0 & 0 & 0 & 0 & 0 & 0 \\ 0 & 1-b_1 & 0 & 0 & 0 & 0 & b_1 & 0 & 0 \\ 0 & 0 & 1-b_2 & 0 & 0 & 0 & 0 & b_2 & 0 \\ 0 & 0 & 0 & f & 1-f & 0 & 0 & 0 & 0 \\ 0 & a_1 & 0 & 0 & 0 & 0 & 1-a_1 & 0 & 0 \\ 0 & 0 & a_2 & 0 & 0 & 0 & 0 & 1-a_2 & 0 \\ 0 & 0 & 0 & 0 & 0 & b_3 & 0 & 0 & 1-b_3 \end{pmatrix} \begin{pmatrix} T_1 \\ T_2 \\ T_3 \\ T_4 \\ T_5 \\ T_6 \\ T_7 \\ T_9 \\ T_{11} \end{pmatrix} \quad (25)$$

To facilitate calculations, Eq. (25) has been reformulated based on the internal and outlet nodes:

$$\begin{pmatrix} \mathbf{T}_{\text{internal}} \\ \mathbf{T}_{\text{out}} \end{pmatrix} = \begin{pmatrix} \mathbf{H}_{m,r}^{1,1} & \mathbf{H}_{m,r}^{1,2} \\ \mathbf{H}_{m,r}^{2,1} & \mathbf{H}_{m,r}^{2,2} \end{pmatrix} \begin{pmatrix} \mathbf{T}_{\text{internal}} \\ \mathbf{T}_{\text{in}} \end{pmatrix} \quad (26)$$

where  $\mathbf{H}_{m,r}$  represents the reduced version of  $\mathbf{H}_r$ , and the dimensions of blocks  $\mathbf{H}_{m,r}^{j,i}$  align with those of  $\mathbf{T}_{\text{in}}$ ,  $\mathbf{T}_{\text{out}}$ , and  $\mathbf{T}_{\text{internal}}$ .

Furthermore, Eq. (26) can be decomposed into two equations using block matrix multiplication. After rearranging these two equations, the system's thermodynamic equation is derived as follows:

$$\begin{cases} (\mathbf{I} - \mathbf{H}_{m,r}^{1,1}) \mathbf{T}_{\text{internal}} = \mathbf{H}_{m,r}^{1,2} \mathbf{T}_{\text{in}} \\ \mathbf{T}_{\text{out}} = \mathbf{H}_{m,r}^{2,1} \mathbf{T}_{\text{internal}} + \mathbf{H}_{m,r}^{2,2} \mathbf{T}_{\text{in}} \end{cases} \quad (27)$$

By substituting Eq. (27) into each element and expanding, the following can be obtained:

$$\begin{pmatrix} 1 & 0 & 0 & 0 & 0 & a_3 - 1 \\ -1 & 1 & 0 & 0 & 0 & 0 \\ -1 & 0 & 1 & 0 & 0 & 0 \\ 0 & b_1 - 1 & 0 & 1 & 0 & 0 \\ 0 & 0 & b_2 - 1 & 0 & 1 & 0 \\ 0 & 0 & 0 & -f & f - 1 & 1 \end{pmatrix} \begin{pmatrix} T_1 \\ T_2 \\ T_3 \\ T_4 \\ T_5 \\ T_6 \end{pmatrix} = \begin{pmatrix} a_3 T_{11} \\ 0 \\ 0 \\ b_1 T_7 \\ b_2 T_9 \\ 0 \end{pmatrix} \quad (28)$$

$$\begin{pmatrix} T_8 \\ T_{10} \\ T_{12} \end{pmatrix} = \begin{pmatrix} a_1 T_2 \\ a_2 T_3 \\ b_3 T_6 \end{pmatrix} + \begin{pmatrix} (1 - a_1) T_7 \\ (1 - a_2) T_9 \\ (1 - b_3) T_{11} \end{pmatrix} \quad (29)$$

When the parameters  $a_i$ ,  $b_i$ ,  $f$  and  $T_{in}$  are known, the internal and outlet node temperatures of the multilevel heat exchange system with multifluid can be quickly determined using Eqs. (28) and (29). Furthermore, with the temperatures at each node known, the heat transfer rate between different nodes can also be calculated. In summary, a thermodynamic model of the multilevel heat exchange system with multifluid has been established using the transfer matrix-based method.

#### 4.2. Verification with experimental data

To validate the precision of the above transfer matrix-based multilevel heat exchange system model, the current study uses all the experimental data mentioned in Section 3, focusing on the comparison of temperatures and heat transfer rates. In detail, with the inlet node temperatures ( $T_{in}$ ), mass flow rates of the various working fluids, and the thermal conductivities (KA) of the three HEXs known (using experimental data), the theoretical model is used to calculate the temperatures at internal and outlet nodes and the heat transfer rates between nodes. These results are then compared with experimental data to compute the prediction deviations.

Fig. 13 plots the comparison of the experimental data of the multilevel heat exchange system shown in Fig. 1 with the calculated results using Eq. (28) and Eq. (29). Regarding the inlet and outlet temperatures of HEX-1, HEX-2, and HEX-3, 98.3 %, 97.1 %, and 99.4 % of the data are

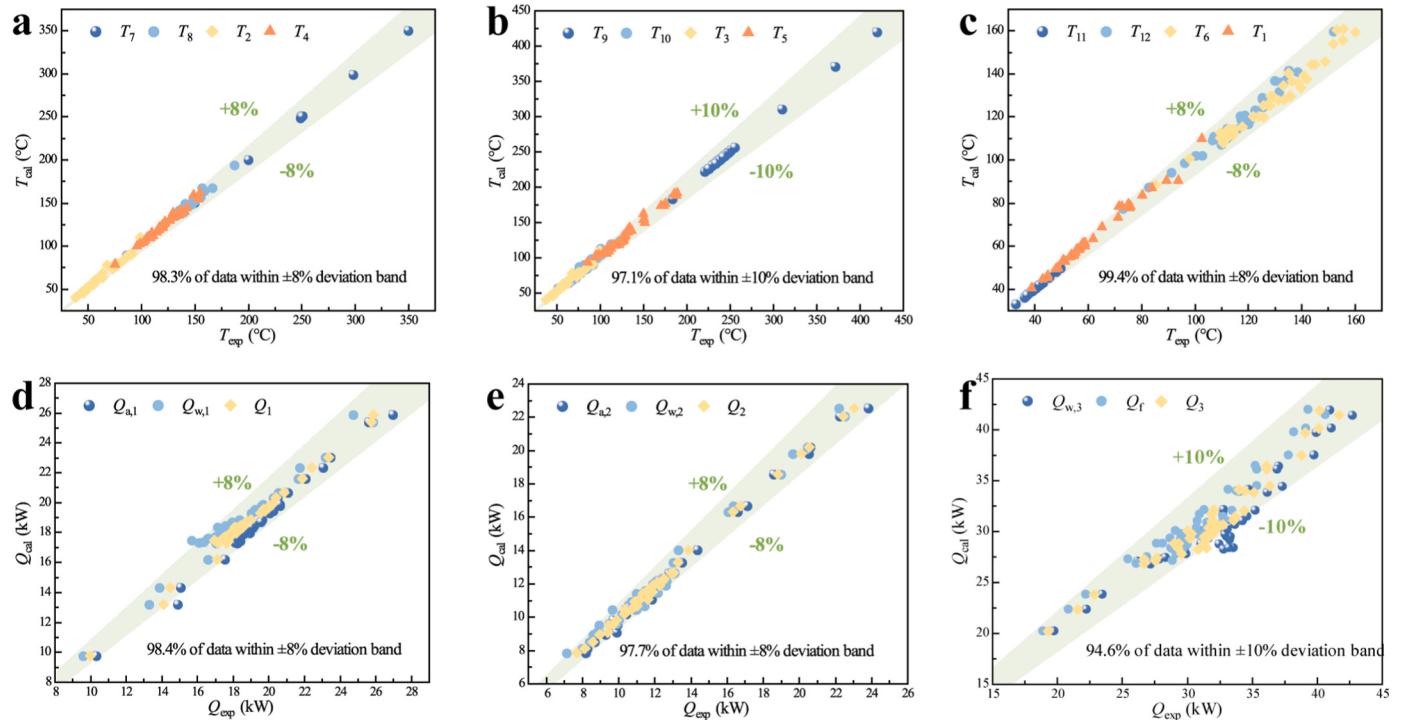
within the error margins of  $\pm 8\%$ ,  $\pm 10\%$ , and  $\pm 8\%$ , respectively. It indicates that the transfer matrix-based model can predict the inlet and outlet temperatures at various nodes within the multilevel heat exchange system with high precision, which is beneficial for temperature monitoring and analysis in aero-engine TMSs, enabling adjustments to be made in line with temperature readings and thermal management strategies. According to Eqs. (1)–(9) and node temperatures calculated by the theoretical model, for HEX-1, HEX-2, and HEX-3, 98.4 %, 97.7 %, and 94.6 % of the heat transfer rate data, respectively, fall within  $\pm 8\%$ ,  $\pm 8\%$ , and  $\pm 10\%$  error bands. It demonstrates that the aforementioned model can also accurately compute the heat transport between different nodes within the system. Consequently, precise energy flow analysis can be conducted for multilevel heat exchange systems, which is also beneficial for optimizing system design.

Fig. 14 summarizes the prediction deviations for all experimental data (774 data points) including temperatures and heat transfer rates, with 97.8 % of the data within  $\pm 10\%$  error bands, thereby validating the transfer matrix-based multilevel heat exchange system model.

#### 4.3. Holistic identification of HEX heat transfer characteristics

Essentially, the above case is a simulation issue, where the KA of each HEX within the system is known in advance, leaving the calculation of node temperatures and heat transfer rates through the model. Nevertheless, in practical operations of a multilevel heat exchange system in an aero engine, the KAs of HEXs vary with flight conditions, whereas the inlet and outlet temperatures of air and fuel ( $T_{in}$  and  $T_{out}$ ) are easier to monitor. Therefore, this research has further developed the transfer matrix-based model by coupling it with the genetic algorithm (GA) [67, 68] to achieve holistic identification of the HEX heat transfer characteristics in practical applications, as illustrated in Fig. 15. When  $T_{in}$ ,  $T_{out}$ , and the mass flow rates of the fluids are known but the KAs of HEXs within the system are unknown, the algorithm developed is used to compute these KAs along with the internal node temperatures ( $T_{internal}$ ).

To validate the overall identification effect of the developed model



**Fig. 13.** The comparison of different parameters of the multilevel heat exchange system (Calculated results vs Experimental data). a: Inlet and outlet temperatures of HEX-1; b: Inlet and outlet temperatures of HEX-2; c: Inlet and outlet temperatures of HEX-3; d: Heat transfer rates of HEX-1; e: Heat transfer rates of HEX-2; f: Heat transfer rates of HEX-3.

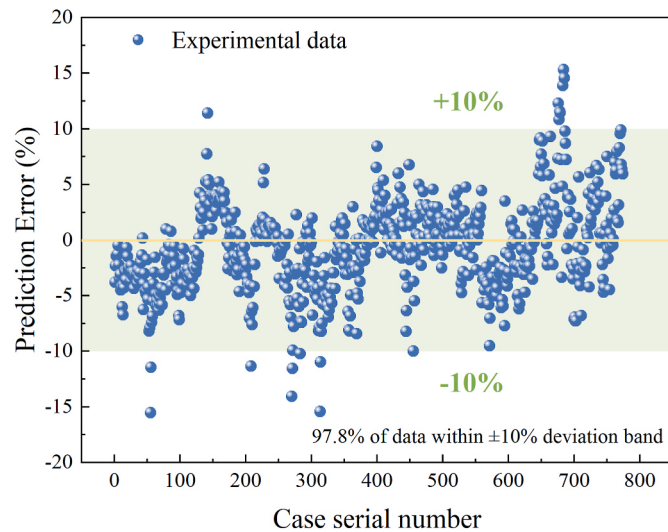


Fig. 14. Prediction errors of all experimental data.

coupled with GA on the heat transfer characteristics of HEXs, the current study conducts comparative calculations using experimental data. Table 9 lists the input parameters for the calculations, while Fig. 15

illustrates the applied calculation procedure. Table 10 presents and compares the calculated thermal conductivities of HEXs and node temperatures within the system to their experimental values. The maximum relative deviation for all parameters is  $-4.79\%$ , indicating that the proposed model coupled with GA can provide results with sufficient accuracy for practical applications in aero-engine multilevel heat exchange systems with multifluid. Besides, Fig. 16 presents the variation of  $KAs$  of different HEXs of the best individual in each generation with respect to the number of generations. It is observed that the value of  $KA$  stabilizes after 20 generations and achieves its optimal value upon meeting the termination condition. Moreover, the algorithm exhibits robustness, as it consistently converges despite substantial deviations from initial values.

Table 9

Input parameters for algorithm validation.

$m_{a,1}$ (kg/s)	$m_{a,2}$ (kg/s)	$m_f$ (kg/s)	$m_{w,1}$ (kg/s)	$m_{w,2}$ (kg/s)	$m_{w,3}$ (kg/s)
0.1973	0.0701	0.1944	0.0600	0.0403	0.1003
$T_7$ (°C)	$T_9$ (°C)	$T_{11}$ (°C)	$T_8$ (°C)	$T_{10}$ (°C)	$T_{12}$ (°C)
249.12	221.48	40.20	147.56	73.35	120.09

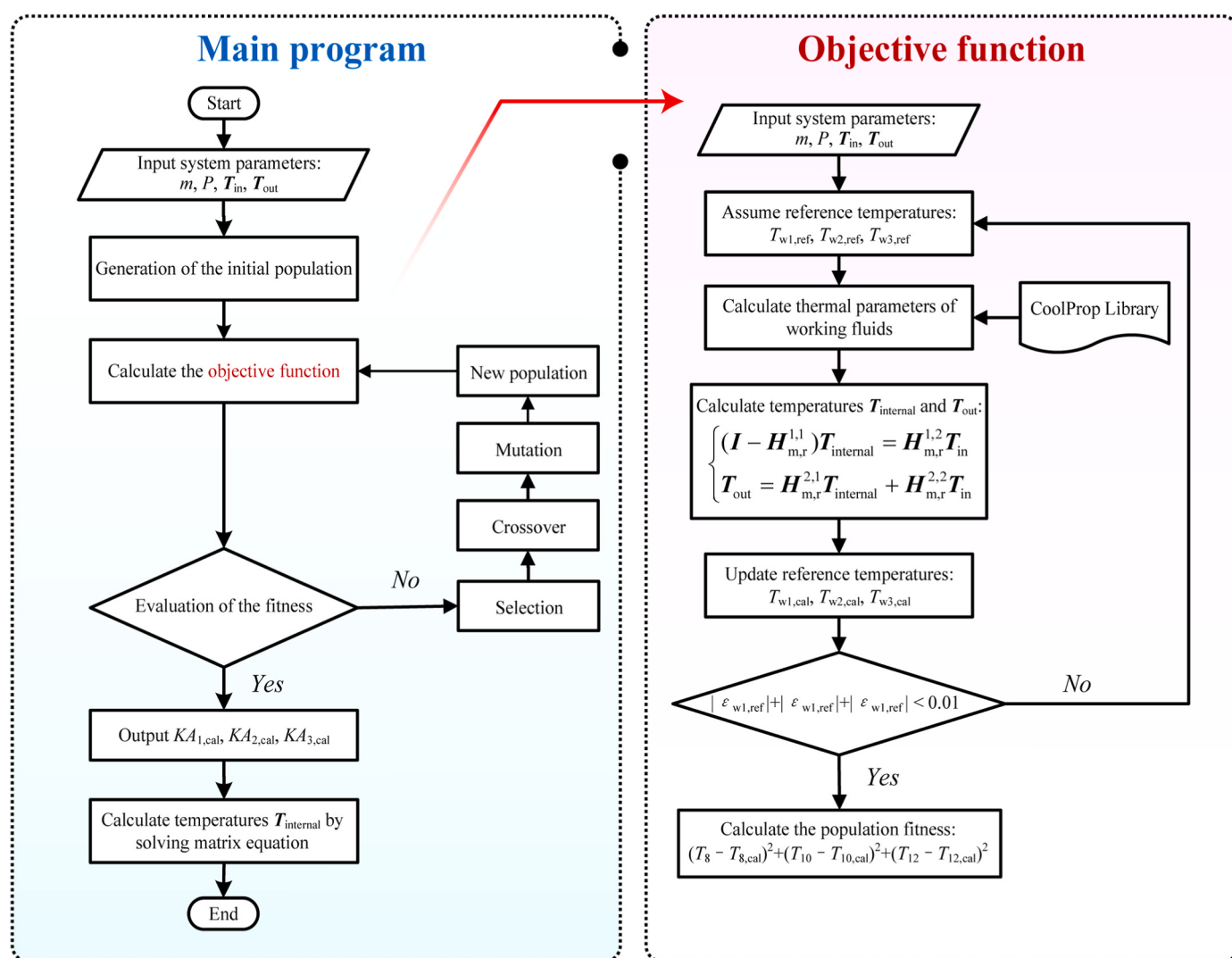
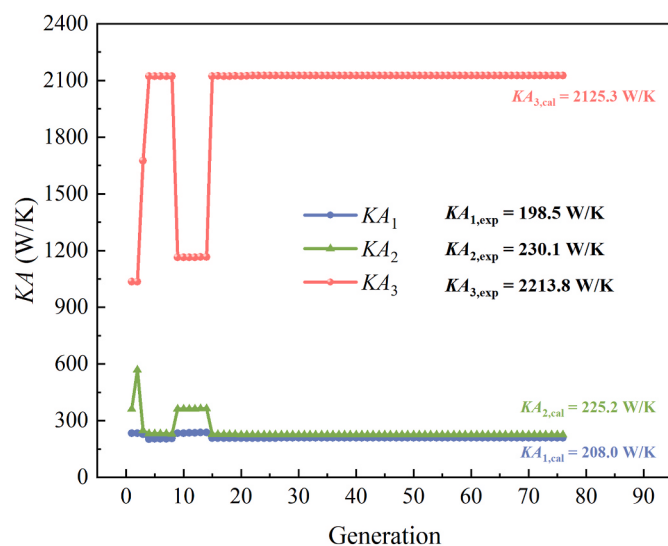


Fig. 15. The flowchart of multilevel heat exchange system calculation with unknown  $KA$  using GA optimization.

**Table 10**  
Calculation results comparison for algorithm validation.

	Experimental value	Calculation value	Error (%)
$T_1$ (°C)	54.81	56.49	−3.07
	55.00	56.49	−2.71
$T_2$ (°C)	54.97	56.49	−2.77
$T_3$ (°C)	135.32	138.72	−2.51
$T_4$ (°C)	122.64	119.06	2.92
$T_5$ (°C)	135.84	130.83	3.69
$T_6$ (°C)	147.56	146.42	0.77
$T_8$ (°C)	73.35	72.95	0.55
$T_{10}$ (°C)	120.09	117.53	2.13
$T_{12}$ (°C)	198.5	208.0	−4.79
$KA_1$ (W/K)	230.1	225.2	2.13
$KA_2$ (W/K)	2213.8	2125.3	4.00
$KA_3$ (W/K)			



**Fig. 16.** Variation of the  $KA$  of different HEXs of the best individual in each generation with respect to the number of generations.

## 5. Conclusions

This study experimentally investigates the thermodynamic characteristics of a multilevel heat exchange system with multifluid for aero engines. An experimental platform integrating compressor bleed air, bearing cavity cooling air, aviation kerosene, and high-pressure water was constructed. The effects of working fluid mass flow rates, inlet temperatures, and water flow distribution ratios on system performance were evaluated, and corresponding thermal management strategies were proposed. A mathematical model, enhanced by genetic algorithm (GA) coupling, was developed and validated with experimental data, achieving high accuracy in the holistic identification of the HEX heat transfer performance. The primary findings are summarized as follows:

- Variations in thermal energy input to a HEX on one branch of a multilevel heat exchange system have minimal influence on other branches.
- The intermediate working fluid serves solely as a thermal energy transfer medium. Adjusting its mass flow rate or distribution ratio alters the thermal transfer rate and internal node temperatures without affecting the system's total heat transfer rate.  $Q_1$  and  $Q_2$  undergo slight changes with variations in  $\xi$ , but their sum theoretically remains constant ( $Q_3$ ).
- When regulating  $m_{a,1}$  or  $m_{a,2}$ , attention should be given to  $T_4$  or  $T_5$ , respectively. The regulation of  $m_f$  has a governing effect on the temperatures of all working fluids in the system, but it also affects combustion characteristics. Therefore, adjustments to  $m_f$  should be synchronized with combustion requirements. Changes in flight parameters can enhance system heat absorption but require careful monitoring of critical temperatures (e.g.,  $T_{12}$ ,  $T_4$ , and  $T_5$ ).
- The transfer matrix-based model achieved high accuracy, capturing 97.8 % of the experimental data within a  $\pm 10$  % error margin. For practical applications in aero engines, the developed model coupled with GA effectively identifies HEX heat transfer characteristics, exhibiting a maximum relative deviation of −4.79 %.

The current work focuses solely on steady-state analysis and modeling of the multilevel heat exchange system. In future work, we plan to expand our analysis to explore the effects of multi-parameter coupling on system characteristics and to conduct dynamic modeling and analysis of the multilevel heat exchange system with multifluid.

## CRediT authorship contribution statement

**Weitong Liu:** Writing – original draft, Software, Investigation, Formal analysis, Data curation. **Guoqiang Xu:** Conceptualization. **Xiuting Gu:** Resources. **Jingshuai Yao:** Resources. **Mowen Li:** Supervision. **Ming Lei:** Supervision. **Qun Chen:** Writing – review & editing, Methodology. **Yanchen Fu:** Writing – review & editing, Project administration, Methodology, Funding acquisition.

## Declaration of generative AI and AI-assisted technologies in the writing process

During the preparation of this work, the author(s) used Youdao AIBox and ChatGPT in order to check grammar and improve readability. The author(s) did not use this tool/service to directly generate the manuscript but only to polish the manuscript written by the author(s). After using this tool/service, the author(s) reviewed and edited the content as needed and take(s) full responsibility for the content of the publication.

## Declaration of competing interest

The authors declare that they have no known competing financial interests or personal relationships that could have appeared to influence the work reported in this paper.

## Acknowledgment

The authors appreciate the supports from the Beijing Nova Program (No. 20240484560), Beijing Municipal Science & Technology Commission, Administrative Commission of Zhongguancun Science Park (No. Z241100007424005).

## Appendix A. Experimental data

This appendix gives the experimental data for the various cases.

### A.1. Experimental data of HEX-1

	$m_{a,1}$ (kg/s)	$m_{w,1}$ (kg/s)	$T_7$ (°C)	$T_8$ (°C)	$T_2$ (°C)	$T_4$ (°C)	$Q_{a,1}$ (kW)	$Q_{w,1}$ (kW)	$Q_1$ (kW)
$m_{a,1}$ variation	0.1599	0.0620	249.71	132.84	50.36	119.03	19.13	17.86	18.50
	0.1806	0.0623	249.91	141.03	53.00	126.51	20.14	19.24	19.69
	0.1983	0.0639	249.95	146.11	55.30	131.92	21.10	20.57	20.83
	0.2173	0.0639	249.93	150.81	56.00	136.70	22.08	21.69	21.88
	0.2404	0.0640	250.64	155.37	56.23	142.32	23.49	23.19	23.34
	0.2999	0.0640	249.64	166.42	58.04	153.86	25.62	25.86	25.74
$m_{a,2}$ variation	0.1973	0.0600	249.12	147.56	55.00	135.32	20.54	20.27	20.40
	0.1923	0.0590	250.01	147.94	55.56	135.25	20.11	19.78	19.94
	0.1998	0.0590	250.36	149.66	56.50	135.45	20.62	19.59	20.11
	0.1991	0.0590	250.66	149.50	57.33	136.66	20.64	19.69	20.17
	0.1962	0.0590	249.80	149.07	57.89	135.62	20.26	19.29	19.78
	0.1931	0.0590	250.01	148.67	58.58	135.25	20.06	19.03	19.54
$m_f$ variation	0.1582	0.0640	250.07	132.47	49.00	116.37	19.05	18.08	18.56
	0.1597	0.0640	249.89	132.80	50.30	117.03	19.14	17.92	18.53
	0.1586	0.0640	251.08	134.77	53.63	119.75	18.88	17.76	18.32
	0.1564	0.0620	250.56	135.63	56.50	122.01	18.40	17.06	17.73
	0.1597	0.0640	251.23	139.65	63.84	127.23	18.25	17.06	17.65
	0.1571	0.0640	250.70	141.52	67.80	129.52	17.57	16.62	17.10
$m_{w,3}$ variation	0.1580	0.0630	249.08	157.08	98.67	148.49	14.91	13.31	14.11
	0.1624	0.2211	250.34	141.32	91.30	108.19	18.13	15.72	16.92
	0.1600	0.1980	250.93	140.33	88.70	108.32	18.13	16.35	17.24
	0.1593	0.1740	250.33	139.31	85.54	107.55	18.11	16.11	17.11
	0.1595	0.1490	250.65	138.86	82.53	109.03	18.26	16.60	17.43
	0.1580	0.1240	250.00	138.03	78.20	110.82	18.12	17.01	17.56
$T_7$ variation	0.1609	0.1000	250.24	137.89	73.00	114.22	18.51	17.33	17.92
	0.1594	0.0750	251.04	137.12	63.20	120.00	18.59	17.90	18.25
	0.1587	0.0450	250.21	139.77	45.85	140.79	17.94	17.96	17.95
	0.1589	0.0618	150.22	86.01	37.89	75.05	10.34	9.60	9.97
	0.1606	0.0620	200.33	108.11	41.95	95.49	15.08	13.89	14.48
	0.1591	0.0620	250.17	133.51	47.60	117.40	19.00	18.15	18.57
$T_9$ variation	0.1605	0.0620	298.81	159.18	53.64	137.12	23.09	21.76	22.43
	0.1591	0.0605	350.43	187.10	58.20	155.15	26.99	24.75	25.87
	0.1624	0.0600	249.89	131.69	43.60	116.59	19.65	18.36	19.00
	0.1593	0.0610	249.77	133.92	46.86	118.36	18.89	18.29	18.59
	0.1598	0.0610	250.21	135.81	50.30	119.69	18.72	17.76	18.24
	0.1596	0.0610	249.97	136.94	52.70	120.31	18.47	17.30	17.89
$\xi$ variation	0.1595	0.0616	249.83	138.16	55.80	122.36	18.24	17.22	17.73
	0.1625	0.1199	250.76	136.80	75.14	109.68	18.96	17.40	18.18
	0.1607	0.1310	250.42	137.11	76.70	108.10	18.64	17.29	17.96
	0.1613	0.1450	251.43	136.54	76.80	105.53	18.98	17.50	18.24
	0.1624	0.1570	251.26	135.85	77.00	103.71	19.19	17.61	18.40
	0.1618	0.1650	250.26	135.34	77.00	101.75	19.04	17.15	18.10
	0.1634	0.1800	250.41	133.54	75.00	98.79	19.55	17.97	18.76

### A.2. Experimental data of HEX-2

	$m_{a,2}$ (kg/s)	$m_{w,2}$ (kg/s)	$T_9$ (°C)	$T_{10}$ (°C)	$T_3$ (°C)	$T_5$ (°C)	$Q_{a,2}$ (kW)	$Q_{w,2}$ (kW)	$Q_2$ (kW)
$m_{a,1}$ variation	0.0702	0.0402	243.24	64.07	50.14	127.51	12.80	13.05	12.93
	0.0703	0.0402	233.60	67.07	52.90	127.82	11.91	12.65	12.28
	0.0694	0.0407	231.10	68.75	55.21	126.55	11.46	12.20	11.83
	0.0685	0.0407	247.89	68.88	55.99	129.22	12.49	12.52	12.51
	0.0680	0.0406	236.90	69.14	56.20	127.04	11.61	12.08	11.85
	0.0661	0.0404	252.09	69.63	58.09	128.93	12.29	12.03	12.16
$m_{a,2}$ variation	0.0701	0.0403	221.48	73.35	54.97	122.64	10.56	11.45	11.01
	0.1053	0.0410	241.72	82.13	55.50	150.29	17.13	16.38	16.75
	0.1439	0.0409	235.16	95.15	56.50	170.31	20.54	19.68	20.11
	0.1614	0.0408	230.07	104.69	57.40	175.86	20.65	20.48	20.56
	0.1862	0.0411	238.68	113.35	57.90	185.44	23.83	22.21	23.02
	0.2139	0.0410	226.21	124.23	58.60	188.34	22.28	22.56	22.42
$m_f$ variation	0.0700	0.0406	236.00	65.09	48.90	123.27	12.17	12.67	12.42
	0.0708	0.0405	252.20	64.71	50.30	127.11	13.52	13.06	13.29
	0.0708	0.0405	238.42	67.20	53.60	126.53	12.33	12.42	12.37
	0.0706	0.0424	248.81	68.68	56.52	130.05	12.94	13.11	13.02
	0.0710	0.0406	238.95	73.92	63.85	132.42	11.94	11.72	11.83
	0.0713	0.0406	239.92	76.69	67.87	134.41	11.86	11.36	11.61
	0.0706	0.0404	239.34	101.50	99.10	150.50	9.92	8.81	9.37

(continued on next page)

(continued)

	$m_{a,2}$ (kg/s)	$m_{w,2}$ (kg/s)	$T_9$ (°C)	$T_{10}$ (°C)	$T_3$ (°C)	$T_5$ (°C)	$Q_{a,2}$ (kW)	$Q_{w,2}$ (kW)	$Q_2$ (kW)
$m_{w,3}$ variation	0.0704	0.1440	224.94	92.32	91.50	107.85	9.51	9.91	9.71
	0.0698	0.1293	247.07	91.34	88.90	108.60	11.08	10.72	10.90
	0.0697	0.1142	244.05	89.08	85.74	108.41	11.02	10.89	10.96
	0.0702	0.0987	238.78	87.58	82.83	109.57	10.82	11.10	10.96
	0.0701	0.0829	233.72	85.26	78.40	110.32	10.60	11.13	10.86
	0.0709	0.0682	244.29	83.14	73.20	113.35	11.64	11.52	11.58
	0.0711	0.0518	242.53	78.11	63.31	118.17	11.91	11.94	11.92
	0.0708	0.0303	225.80	91.07	45.76	124.81	9.71	10.05	9.88
$T_7$ variation	0.0622	0.0401	256.08	82.87	37.60	95.31	10.98	9.67	10.33
	0.0620	0.0401	249.06	91.41	41.70	95.05	9.97	8.95	9.46
	0.0614	0.0399	246.60	98.05	47.50	98.99	9.30	8.60	8.95
	0.0606	0.0400	237.51	96.70	53.55	103.80	8.70	8.42	8.56
	0.0605	0.0412	235.29	101.10	58.02	104.40	8.28	8.01	8.15
$T_9$ variation	0.0614	0.0400	183.75	52.16	43.35	86.07	8.19	7.15	7.67
	0.0613	0.0398	247.58	60.17	46.60	112.68	11.69	11.01	11.35
	0.0609	0.0391	310.70	79.93	50.30	131.30	14.40	13.31	13.86
	0.0609	0.0387	371.25	107.19	52.50	151.31	16.60	16.10	16.35
	0.0613	0.0380	419.81	128.04	55.77	174.09	18.59	19.01	18.80
$\xi$ variation	0.0691	0.0809	244.66	77.95	75.26	109.06	11.73	11.49	11.61
	0.0681	0.0689	246.11	81.36	76.80	116.52	11.43	11.51	11.47
	0.0694	0.0543	244.88	83.62	76.95	125.84	11.41	11.18	11.29
	0.0702	0.0441	242.85	85.82	77.00	136.77	11.24	11.12	11.18
	0.0703	0.0344	235.12	89.90	76.80	152.39	10.40	11.00	10.70
	0.0694	0.0210	244.60	96.91	75.10	188.99	10.46	10.19	10.32

## A.3. Experimental data of HEX-3

	$m_{w,3}$ (kg/s)	$m_f$ (kg/s)	$T_6$ (°C)	$T_1$ (°C)	$T_{11}$ (°C)	$T_{12}$ (°C)	$Q_{w,3}$ (kW)	$Q_f$ (kW)	$Q_3$ (kW)
$m_{a,1}$ variation	0.1024	0.1954	127.35	50.66	36.86	112.05	32.97	30.80	31.89
	0.1026	0.1951	133.37	53.20	38.72	118.12	34.59	32.76	33.67
	0.1042	0.1950	135.67	55.17	39.93	120.70	35.28	33.44	34.36
	0.1042	0.1949	138.62	56.05	40.63	122.68	36.21	34.04	35.13
	0.1043	0.1948	141.95	56.96	40.75	125.80	37.32	35.38	36.35
	0.1044	0.1949	148.94	58.51	41.54	131.79	39.79	37.82	38.80
	0.1003	0.1944	135.84	54.81	40.20	120.09	34.24	32.96	33.60
	0.1002	0.1944	143.50	55.69	40.56	125.54	37.04	35.26	36.15
$m_{a,2}$ variation	0.1001	0.1944	151.91	57.23	40.84	132.26	39.98	38.20	39.09
	0.0999	0.1943	155.40	57.85	41.24	134.63	41.13	39.12	40.12
	0.0998	0.1941	155.78	58.40	41.56	135.36	41.02	39.29	40.16
	0.1001	0.1943	160.06	58.93	41.96	138.59	42.75	40.66	41.70
	0.1043	0.2503	125.62	48.68	42.00	102.98	33.68	31.88	32.78
$m_f$ variation	0.1044	0.2270	125.70	51.06	41.62	106.73	32.73	30.98	31.86
	0.1044	0.2026	128.10	53.75	41.07	112.95	32.60	30.70	31.65
	0.1044	0.1796	128.40	57.89	40.64	117.17	30.93	29.10	30.01
	0.1043	0.1541	133.17	65.09	40.10	125.54	29.90	28.09	29.00
	0.1044	0.1313	134.93	71.51	39.70	130.18	27.89	25.45	26.67
$m_{w,3}$ variation	0.1035	0.0834	153.31	102.74	37.70	152.25	22.24	20.88	21.56
	0.3651	0.1946	110.72	93.68	39.24	109.93	26.22	28.86	27.54
	0.3272	0.1946	111.06	89.43	39.33	109.81	29.80	28.78	29.29
	0.2882	0.1947	110.93	83.85	39.15	109.76	32.82	28.83	30.83
	0.2478	0.1946	112.51	80.31	39.18	110.94	33.56	29.33	31.44
	0.2070	0.1947	114.07	75.91	39.10	111.84	33.21	29.76	31.48
	0.1684	0.1946	117.84	71.34	39.10	114.32	32.92	30.84	31.88
	0.1268	0.1944	123.83	61.77	39.33	115.94	33.08	31.45	32.26
$T_7$ variation	0.0751	0.1946	139.69	44.90	39.75	111.01	29.94	29.15	29.54
	0.1017	0.2358	85.38	38.87	33.10	73.06	19.78	18.86	19.32
	0.1020	0.2353	97.83	42.84	36.23	82.71	23.47	22.21	22.84
	0.1022	0.2346	114.77	48.60	40.80	96.16	28.35	26.90	27.62
	0.1020	0.2338	131.19	54.73	45.80	109.61	32.77	31.51	32.14
$T_9$ variation	0.1016	0.2333	140.75	58.76	49.82	117.59	35.09	33.80	34.44
	0.1003	0.2353	109.55	44.86	37.23	91.29	27.19	26.11	26.65
	0.1005	0.2349	121.91	47.92	39.97	100.38	31.19	29.50	30.34
	0.1002	0.2345	129.40	51.38	43.12	106.74	32.82	31.32	32.07
	0.0997	0.2344	136.56	53.67	45.30	112.19	34.73	33.18	33.96
$\xi$ variation	0.0994	0.2340	145.05	56.80	48.12	118.81	36.93	35.35	36.14
	0.2004	0.1953	112.58	74.98	40.20	110.16	31.68	28.70	30.19
	0.1997	0.1952	114.51	74.86	39.95	111.82	33.30	29.52	31.41
	0.1991	0.1953	114.63	75.17	39.89	111.96	33.04	29.61	31.33
	0.2007	0.1951	114.29	74.81	39.67	111.69	33.32	29.55	31.43
	0.1992	0.1952	114.56	75.78	39.64	112.77	32.48	30.05	31.27
	0.2006	0.1952	109.60	72.77	39.64	107.30	31.05	27.65	29.35

## Data availability

Data will be made available on request.

## References

- [1] Flaherty KW, Andrews KM, Liston GW. Operability benefits of airbreathing hypersonic propulsion for flexible access to space. *J Spacecraft Rockets* 2010;47(2):280–7.
- [2] Wang C, Yu X, Pan X, Qin J, Huang H. Thermodynamic optimization of the indirect precooled engine cycle using the method of cascade utilization of cold sources. *Energy* 2022;238.
- [3] van Heerden ASJ, Judd DM, Jafari S, Lawson CP, Nikolaidis T, Bosak D. Aircraft thermal management: practices, technology, system architectures, future challenges, and opportunities. *Prog Aero Sci* 2022;128.
- [4] Fu Y, Liu Y, Wang J, Wang Y, Xu G, Wen J. Local resistance characteristics of elbows for supercritical pressure RP-3 flowing in serpentine micro-tubes. *Propul Power Res* 2024;13:245–56.
- [5] Zhang S, Li X, Zuo J, Qin J, Cheng K, Feng Y, et al. Research progress on active thermal protection for hypersonic vehicles. *Prog Aero Sci* 2020;119.
- [6] Fu Y, Liu W, Wang J, Zhang L, Wen J, Wu H, et al. Experimental investigation on heat transfer enhancement of supercritical pressure aviation kerosene in tubular laminar flow by vibration. *Appl Therm Eng* 2024;257.
- [7] Welge R. N+2 supersonic concept development and systems integration. 2010. NASA/CR-2010-216842.
- [8] Abdalla AM, Hossain S, Nisifordi OB, Azad AT, Dawood M, Azad AK. Hydrogen production, storage, transportation and key challenges with applications: a review. *Energy Convers Manag* 2018;165:602–27.
- [9] Togawa M, Aoki T, Hirakoshi H, Ito T. A concept of LACE for SSTO space plane. 3rd International Aerospace Planes Conference 2013;5011.
- [10] Varvill R, Bond A. A comparison of propulsion concepts for SSTO reusable launchers. *J Br Interplanet Soc (JBIS)* 2003;56(3/4):108–17.
- [11] Escher WJ. Cryogenic hydrogen-induced air-liquefaction technologies for combined-cycle propulsion applications. NASA. Lewis Research Center, Rocket-Based Combined-Cycle (RBCC). Propulsion Technology Workshop. Tutorial Session. 1992.
- [12] Hemsell C. Hotol's Secret Engines Revealed. The technical details of Hotol's RB545 airbreathing engine. *Spaceflight* 1993;35.
- [13] Rudakov A, Balepin V. Propulsion systems with air precooling for aerospaceplane. SAE Technical Paper 1991. No. 911182.
- [14] Balepin V. High speed propulsion cycles. In: *Advances on propulsion technology for high-speed aircraft* educational notes RTO-EN-AVT-150 Neuilly-sur-Seine; 2007. France: RTO.
- [15] Bruening GB, Chang WS. Cooled cooling air systems for turbine thermal management. Conference Cooled cooling air systems for turbine thermal management, 78606. American Society of Mechanical Engineers; 1999.
- [16] Liu W, Xu G, Fu Y, Wen J, Zhang N. Numerical investigation on forced, natural, and mixed convective heat transfer of n-decane in laminar flow at supercritical pressures. *Int J Heat Mass Tran* 2023;209.
- [17] Baltman E, Tai JC, Shi M, Mavris DN. An investigation of cooled cooling air for a Mach 2.2 commercial supersonic transport. *AIAA Propuls Energy* 2021. Forum 2021;3492.
- [18] Chepkin V. New generation of Russian aircraft engines conversion and future goals. ISABE paper 1999:99–7042.
- [19] Chen M, Zhang J, Tang H. Performance analysis of a three-stream adaptive cycle engine during throttling. *Int J Aerosp Eng* 2018;2018.
- [20] Rolt AM, Kyprianidis K. Assessment of new aero engine core concepts and technologies in the EU framework 6 NEWAC programme. Conference Assessment of new aero engine core concepts and technologies in the EU framework 6 NEWAC programme.
- [21] Huang H, Spadaccini LJ, Sobel D. Fuel-cooled thermal management for advanced aeroengines. *J Eng Gas Turbines Power* 2004;126(2):284–93.
- [22] Herring NR, Heister SD. Review of the development of compact, high performance heat exchangers for gas turbine applications 2006;47853:467–76.
- [23] Duncan Walker A, Koli B, Guo L, Beecroft P, Zedda M. Impact of a cooled cooling air system on the external aerodynamics of a gas turbine combustion system. *J Eng Gas Turbines Power* 2017;139(5).
- [24] Miller BA. Analysis of several methane-fueled engine cycles for Mach 3.0 flight. 1968. No. NASA-TN-D-4699.
- [25] Boyle RJ, Jones SM. Effects of precooling turbine cooling air on engine performance. In: *Proceedings of Asme Turbo Expo* 2009. 4; 2009. p. 495–504.
- [26] Zhuang L, Xu G, Liu Q, Li M, Dong B, Wen J. Superiority analysis of the cooled cooling air technology for low bypass ratio aero-engine under typical flight mission. *Energy Convers Manag* 2022;259.
- [27] Lee JA, Woods S. Hydrogen embrittlement. TM—2016–218602. Alabama: NASA Marshall Space Flight Center Huntsville; 2016.
- [28] Liu D, Hu J, Yuan X, Zhou L, Zhong X. Failure analysis and experimental verification on the hydrogen-driven pitting corrosion of heat exchanger tube material. *Eng Fail Anal* 2022;137.
- [29] Varvill R, Duran I, Kirk A, Langridge S, Nailard O, Payne R, et al. SABRE technology development: status and update. Conference SABRE technology development: status and update.
- [30] Liewen TC, Yang V. Combustion instabilities in gas turbine engines: operational experience, fundamental mechanisms, and modeling. American Institute of Aeronautics and Astronautics; 2005.
- [31] Cheng Y, Wang Y, Jiang P-X, Zhu Y. Oxidative and pyrolytic coking characteristics of supercritical-pressure n-decane and its influence mechanism on heat transfer. *Fuel* 2024;362.
- [32] Noton M, Swinerd G. Optimization of the rocket-powered ascent of Hotol. *Acta Astronaut* 1989;19(1):17–26.
- [33] Aggarwal R, Lakhara K, Sharma P, Darang T, Jain N, Ganguly S. SABRE ENGINE: single stage to orbit rocket engine. *Int J Innov Res Sci, Eng Technol* 2015;4(10):10360–6.
- [34] Zhang J, Wang Z, Li Q. Thermodynamic efficiency analysis and cycle optimization of deeply precooled combined cycle engine in the air-breathing mode. *Acta Astronaut* 2017;138:394–406.
- [35] Longstaff R, Bond A. The SKYLON project. 17th AIAA International Space Planes and Hypersonic. Systems and Technologies Conference 2011;2244.
- [36] Zhou J, Lu H, Zhang H, Zhao L, Chen J, Zheng R. A preliminary research on a two-stage-to-orbit vehicle with airbreathing pre-cooled hypersonic engines. In: 21st AIAA international space planes and hypersonics technologies conference; 2017.
- [37] Dang C, Xu J, Chen Z, Cheng K, Qin J, Liu G. Comparative study of different layouts in the closed-Brayton-cycle-based segmented cooling thermal management system for scramjets. *Energy* 2024;301.
- [38] Cheng K, Xu J, Dang C, Qin J, Jing W. Performance evaluation of fuel indirect cooling based thermal management system using liquid metal for hydrocarbon-fueled scramjet. *Energy* 2022;260.
- [39] Zhang Z, Wu Z, Luo X, Liu W. Numerical study on convective heat transfer of liquid metal gallium in turbine guide vane. *Aerospace* 2023;10(6).
- [40] Wang C, Yu X, Ha C, Liu Z, Fang J, Qin J, et al. Thermodynamic analysis for a novel chemical precooling turbojet engine based on a multi-stage precooling-compression cycle. *Energy* 2023;262.
- [41] Zhang Z, Cao X, Yang Z, Shao L, Zhang C. Modeling and experimental investigation of an advanced direct-expansion outdoor air dehumidification system. *Appl Energy* 2019;242:1600–12.
- [42] Ang EYM, Ng PS, Soh CB, Wang PC. Multi-stage thermoelectric coolers for cooling wearables. *Therm Sci Eng Prog* 2022;36.
- [43] Buchalik R, Nowak G, Nowak I. Comparative analysis and optimization of one- and two-stage cooling systems with thermoelectric cells with respect to supercooling. *Energy Convers Manag* 2022;259.
- [44] Buchalik R, Nowak G. Optimization of cyclical supercooling in the multi-stage system of a thermoelectric cooler. *Appl Therm Eng* 2023;228.
- [45] Yang B, Wang C, Ji X, Zhang R, Yue X, Nie J. Two-stage evaporative cooling system with composite activated carbon fiber dehumidification. *Int J Therm Sci* 2022;179.
- [46] Fu Y, Liu W, Qi H, Chen Q, Wen J, Xu G. Heat transfer area optimization of intermediate heat-exchange cycle system for aero engines. *Int J Heat Mass Tran* 2024;220.
- [47] Liu W, Xu G, Gang X, Qi H, Li M, Wen J, et al. Theoretical modeling, experimental validation, and thermodynamic analysis on intermediate heat-exchange cycle system. *Int Commun Heat Mass Tran* 2024;156.
- [48] Liu J, Li M, Zhang T, Wang Y, Cao Z, Shao W, et al. Optimization of the aero-engine thermal management system with intermediate cycle based on heat current method. *Appl Therm Eng* 2024;237.
- [49] Liu J, Wang S, Zhang T, Wang Y, He K, Cui Z, et al. Experiment and simulation on a thermal management scheme of intermediate circulation based on heat current method. *Int J Heat Mass Tran* 2023;206.
- [50] Colera M, Soria A, Ballester J. A numerical scheme for the thermodynamic analysis of gas turbines. *Appl Therm Eng* 2019;147:521–36.
- [51] Kamath RS, Biegler LT, Grossmann IE. An equation-oriented approach for handling thermodynamics based on cubic equation of state in process optimization. *Comput Chem Eng* 2010;34(12):2085–96.
- [52] Arnold M. Stability of sequential modular time integration methods for coupled multibody system models. *J Comput Nonlinear Dynam* 2010;5(3).
- [53] Guo Z, Zhu H, Liang X. Entransy—a physical quantity describing heat transfer ability. *Int J Heat Mass Tran* 2007;50(13–14):2545–56.
- [54] Chen Q, Hao J, Zhao T. An alternative energy flow model for analysis and optimization of heat transfer systems. *Int J Heat Mass Tran* 2017;108:712–20.
- [55] Chen Q. Entransy dissipation-based thermal resistance method for heat exchanger performance design and optimization. *Int J Heat Mass Tran* 2013;60:156–62.
- [56] He K, Zhao T, Chen Q, Chen X. Matrix-based network heat transfer modeling approach and its application in thermal system analysis. *Appl Therm Eng* 2020;181.
- [57] Zhao T, Sun Q, Li X, Xin Y, Chen Q. A novel transfer matrix-based method for steady-state modeling and analysis of thermal systems. *Energy* 2023;281.
- [58] Liu Y, Xu G, Fu Y, Wen J, Qi S, Lyu L. Airside pressure drop characteristics of three analogous serpentine tube heat exchangers considering heat transfer for aero-engine cooling. *Chin J Aeronaut* 2022;35(12):32–46.
- [59] Liu W, Xu G, Zhi H, Wang R, Li M, Fu Y. Experimental evaluation of hydrothermal performance in airfoil-fin PCHE with supercritical pressure hydrocarbon fuel. *Int Commun Heat Mass Tran* 2024;159.
- [60] Deng HW, Zhang CB, Xu GQ, Tao Z, Zhang B, Liu GZ. Density measurements of endothermic hydrocarbon fuel at sub- and supercritical conditions. *J Chem Eng Data* 2011;56(6):2980–6.
- [61] Deng HW, Zhu K, Xu GQ, Tao Z, Zhang CB, Liu GZ. Isobaric specific heat capacity measurement for kerosene RP-3 in the near-Critical and supercritical regions. *J Chem Eng Data* 2011;57(2):263–8.

- [62] Bell IH, Wronski J, Quoilin S, Lemort V. Pure and pseudo-pure fluid thermophysical property evaluation and the open-source thermophysical property library CoolProp. *Ind Eng Chem Res* 2014;53(6):2498–508.
- [63] Taylor J. An introduction to error analysis, the study of uncertainties in physical measurements. 1997.
- [64] Zhao T, Min Y, Chen Q, Hao J. Electrical circuit analogy for analysis and optimization of absorption energy storage systems. *Energy* 2016;104:171–83.
- [65] Wang Z, Cao M, Tang H, Ji Y, Han F. A global heat flow topology for revealing the synergistic effects of heat transfer and thermal power conversion in large scale systems: Methodology and case study. *Energy* 2024;290.
- [66] Cao M, Wang Z, Tang H, Li S, Ji Y, Han F. Heat flow topology-driven thermo-mass decoupling strategy: cross-scale regularization modeling and optimization analysis. *Appl Energy* 2024;367.
- [67] Deb K. Multi-objective optimisation using evolutionary algorithms: an introduction. Springer; 2011.
- [68] Gosselin L, Tye-Gingras M, Mathieu-Potvin F. Review of utilization of genetic algorithms in heat transfer problems. *Int J Heat Mass Tran* 2009;52(9–10): 2169–88.